TABLE 1: The Timeline of Creation

Chapter	The Origin of . . .	Measured from the Present (2015)*	Measured from the Big Bang	Mapped to a Single 'Day of Creation'
1	Space, Time and Energy	13.8 Ga	'0'	Midnight
2	Mass	13.8 Ga	10^{-12} s	A fraction after midnight
3	Light	13.8 Ga	380 000 Yrs	2 seconds after midnight
4	Stars and Galaxies	13.5-13.3 Ga	300–550 million Yrs	Between 12:30 to 1:00 am
5	Molecules	10-12 Ga	1.8–3.8 billion Yrs	Between 3:00–6:30 a.m.
6	Solar System }	4.6 Ga	9.2 billion Yrs	About 4 p.m.
7	Earth }			
8	Life	3.5 Ga	10.4 billion Yrs	Almost 6 p.m.
9	Complex Cells and Multicellular Organisms	~2 Ga	11.8 billion Yrs	About 8:30 p.m.
10	Species (Animal Species Diversity)	540 Ma	13.4 billion Yrs	A little after 11:00 p.m.
11	*Homo sapiens*	200 ka	13.8 billion Yrs	About 1 second to midnight
12	Human Consciousness	50 ka	13.8 billion Yrs	About 300 milliseconds to midnight

* Ga = billions of years ago, Ma = millions of years ago, ka = thousands of years ago, Yrs = years, s = seconds. Based on an estimate of the age of the universe of 13.82 billion years established by recent results (21 March 2013) from the European Space Agency's Planck satellite.

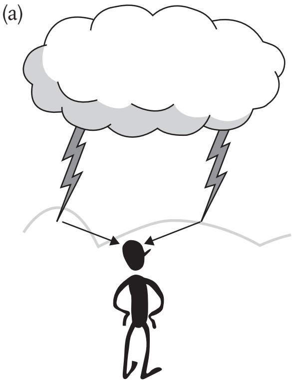

FIGURE 1 The stationary observer in (a) sees the lightning bolts strike simultaneously, as the light from both travels so fast as to appear instantaneous. But the observer in (b), who is moving at a considerable fraction of the speed of light, sees something different. He's moving at half the speed of light from left to right, so by the time the light from the left-hand bolt catches up with him, he's moved a bit further to the right. The light from the right-hand bolt now has less far to travel. Consequently the observer in (b) sees the right-hand bolt strike first.

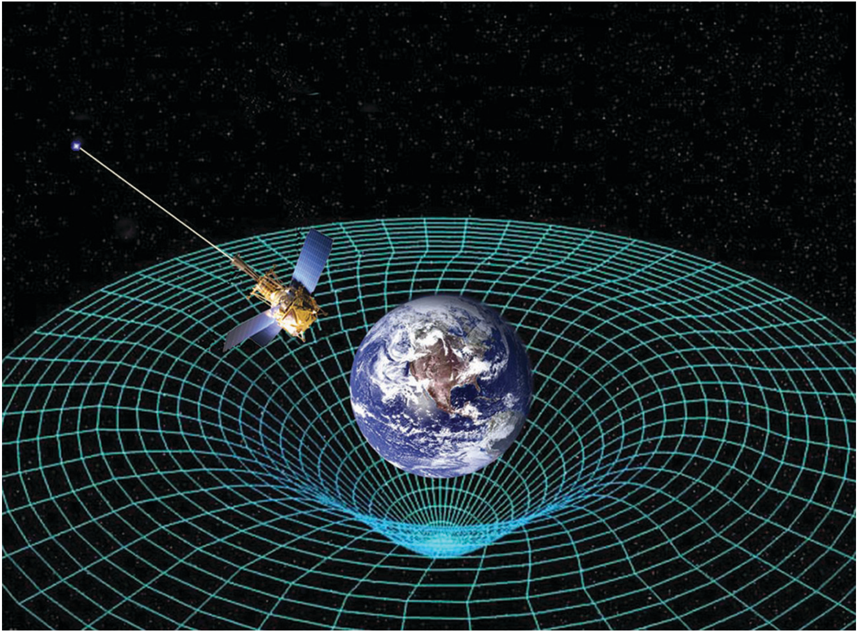

FIGURE 2 Gravity Probe B was launched in April 2004 and measured two phenomena associated with the curvature of spacetime around the Earth. The results were announced in May 2011, and provided a powerful vindication of general relativity. This picture shows the satellite moving in the curved spacetime around the Earth, pointing towards the star IM Pegasi, in the constellation of Pegasus.

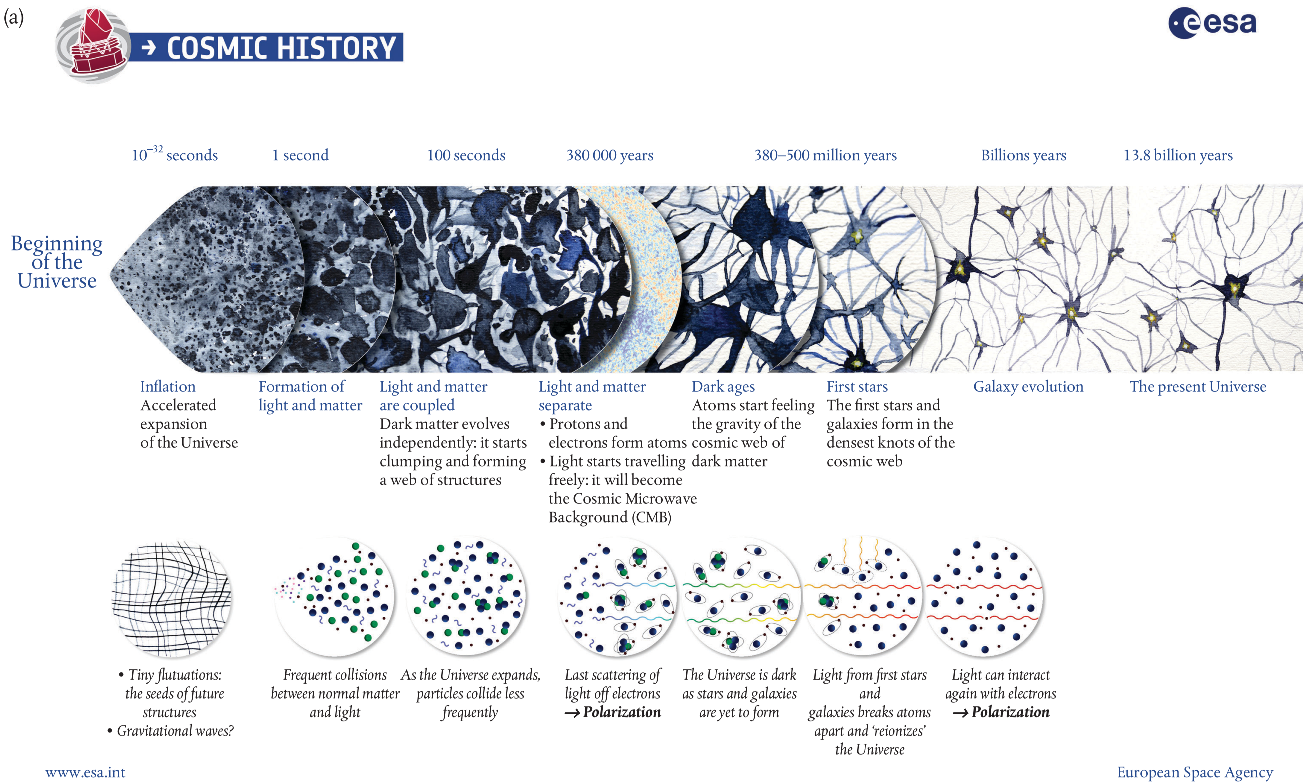

FIGURE 3 (a) A fairly typical way of representing the expansion of the universe from the big bang to the present day.

(b)

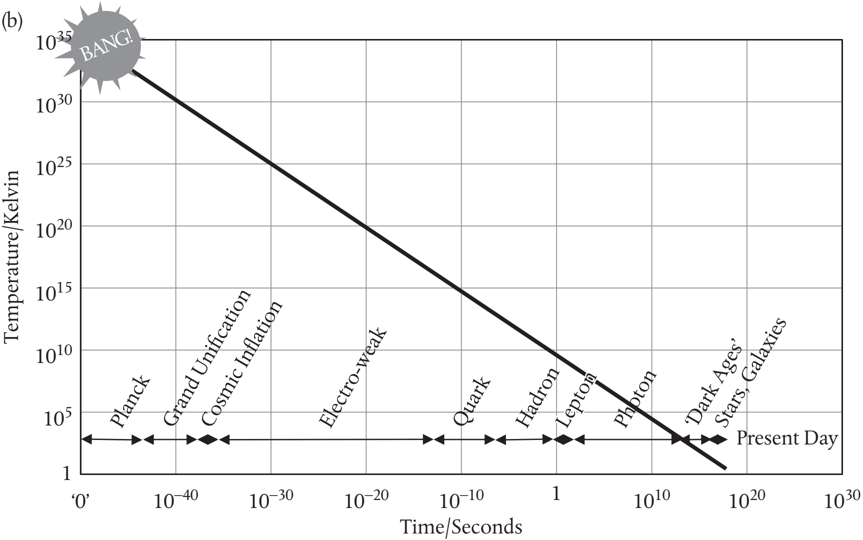
BANG!
Temperature/Kelvin
10^35
10^30
10^25
10^20
10^15
10^10
10^5
1
'0'
10^−40
10^−30
10^−20
10^−10
1
10^10
10^20
10^30
Time/Seconds
Planck
Grand Unification
Cosmic Inflation
Electro-weak
Quark
Hadron
Lepton
Photon
'Dark Ages'
Stars, Galaxies
Present Day

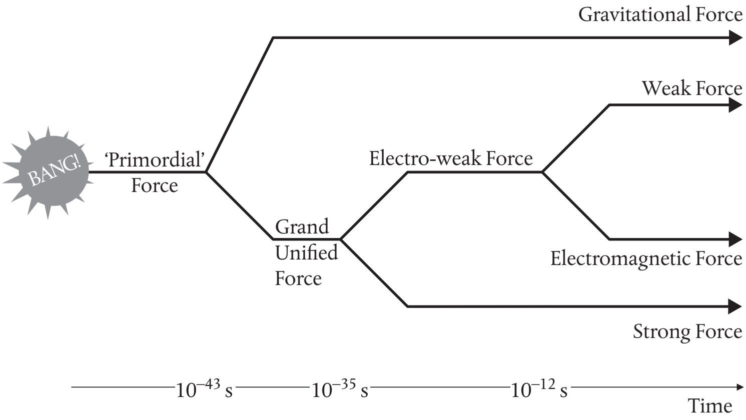

FIGURE 4 At the earliest moments of the big bang, all four forces of nature are thought to be unified in a single, highly symmetric primordial force. After 10^{-43} seconds, the universe undergoes a phase transition, and the force of gravity separates.

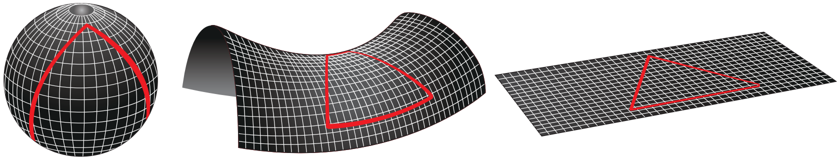

FIGURE 5 The different model universes that Friedmann identified in solutions to Einstein's gravitational field equations produce differently curved spacetimes. The 'closed' universe has a positively curved spacetime as shown in (a). The 'open' universe has a saddle-shaped negatively curved spacetime, (b). A universe with a finely tuned balance between the rate of expansion and the amount of mass-energy it contains will exhibit a flat spacetime, (c).

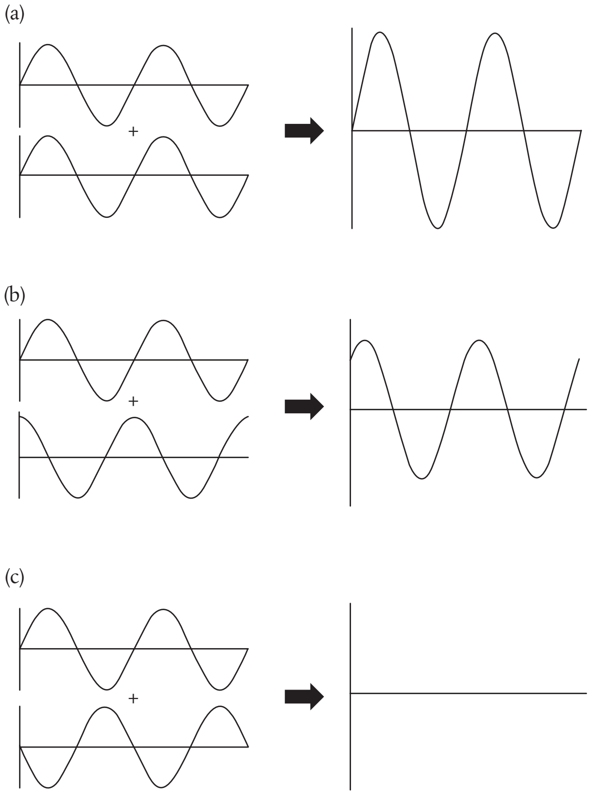

FIGURE 6 When aligned, as in (a), two waves will add and mutually reinforce. This is constructive interference. Moving the waves out of alignment reduces the amplitude, as in (b). If the waves are completely misaligned, the result is destructive interference, (c).

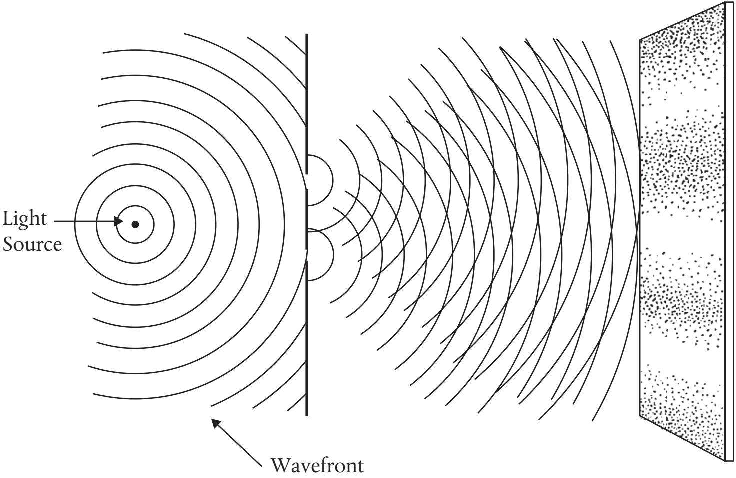

FIGURE 7 When passed through two narrow, closely spaced apertures or slits, light produces a pattern of alternating light and dark fringes. These can be readily explained in terms of a wave theory of light in which overlapping waves interfere constructively (giving rise to a bright fringe) and destructively (dark fringe).

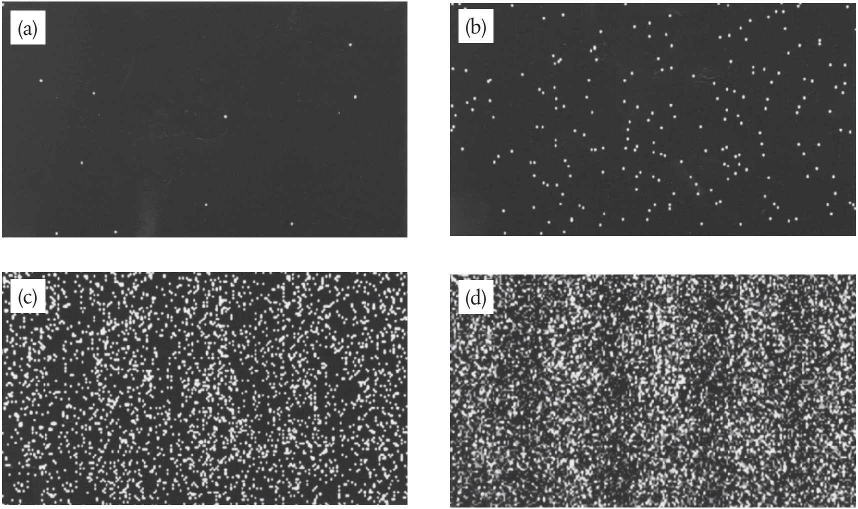

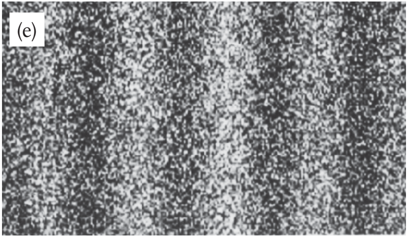

FIGURE 8 We can observe electrons as they pass, one at a time, through a two-slit apparatus, by recording where they strike a piece of photographic film. Each white dot indicates the point where an individual electron is detected. Photos (a)–(e) show the resulting images when, respectively, 10, 100, 3000, 20 000, and 70 000 electrons have been detected. The interference pattern becomes more and more visible as the number of detected electrons increases.

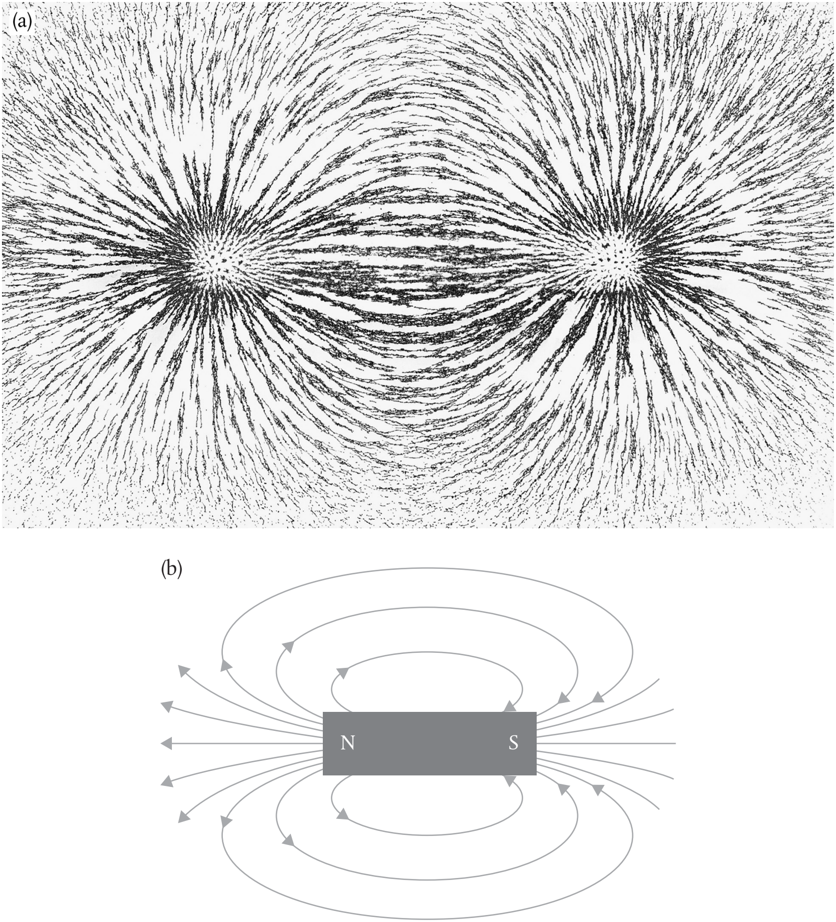

FIGURE 9 (a) Iron filings sprinkled on a sheet of paper held above a bar magnetic reveal the 'lines of force' of the magnetic field stretching between the north and south poles. (b) The pattern of the 'lines of force' is shown schematically here. By convention, the lines of force 'flow' from north to south poles.

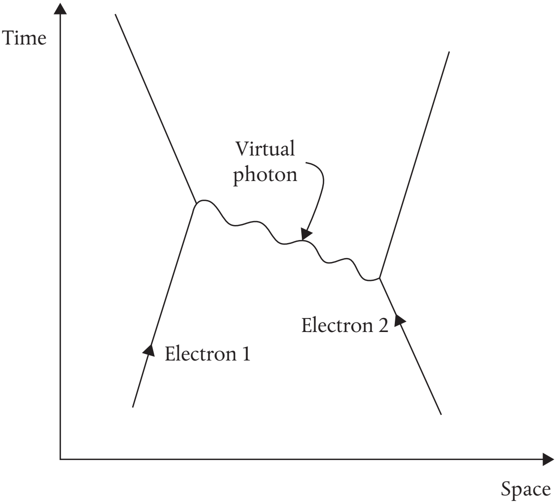

FIGURE 10 This simple diagram represents the interaction between two electrons. Their movement through spacetime is simplified to one dimension of space (shown here along the x-axis) and one of time (y-axis). The electromagnetic force of repulsion between the two negatively charged electrons involves the exchange of a virtual photon at the point of closest approach. The photon is 'virtual' as it is not visible during the interaction.

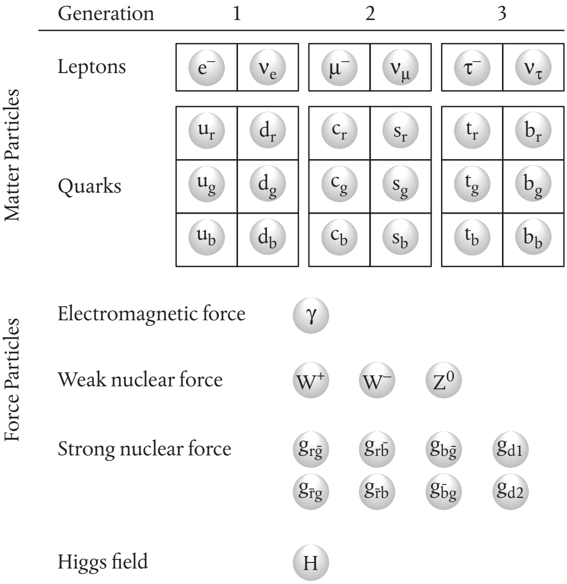

FIGURE 11 The standard model of particle physics describes the interactions of three generations of matter particles through three kinds of force, mediated by a collection of 'force carriers'. The masses of the matter and force particles are determined by their interactions with the Higgs field.

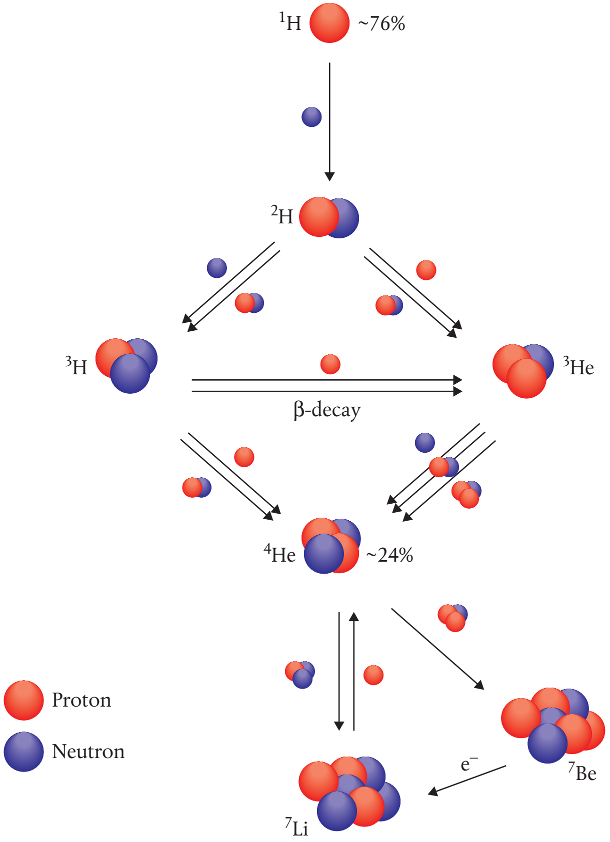

FIGURE 13 Sixteen of the most important nuclear reactions involved in primordial nucleosynthesis. These are shown schematically in terms of the reactions of protons (red balls) and neutrons (blue balls). For simplicity, not all the products of the reactions are shown.

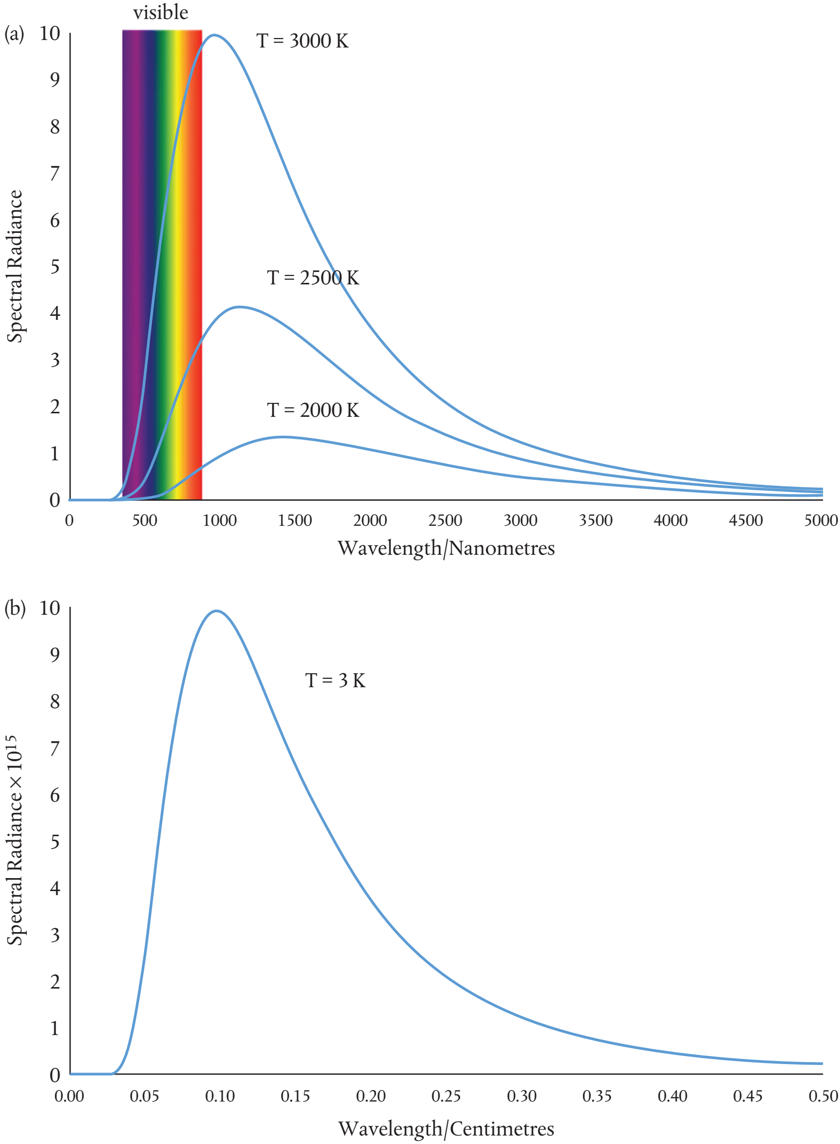

FIGURE 14 A perfect 'black body' emits light with a characteristic pattern of intensity, or spectral radiance, over a distribution of wavelengths determined by the temperature of the body. (a) shows three distributions at temperatures of 3000, 2500, and 2000 kelvin. Note how the spectral radiance sharply declines and the distribution moves to longer wavelengths as the temperature falls. (b) shows the same distribution for a temperature of 3 kelvin, but with the spectral radiance magnified by a factor of 10^{15} compared to (a) and the wavelength axis changed from nanometers to centimetres.

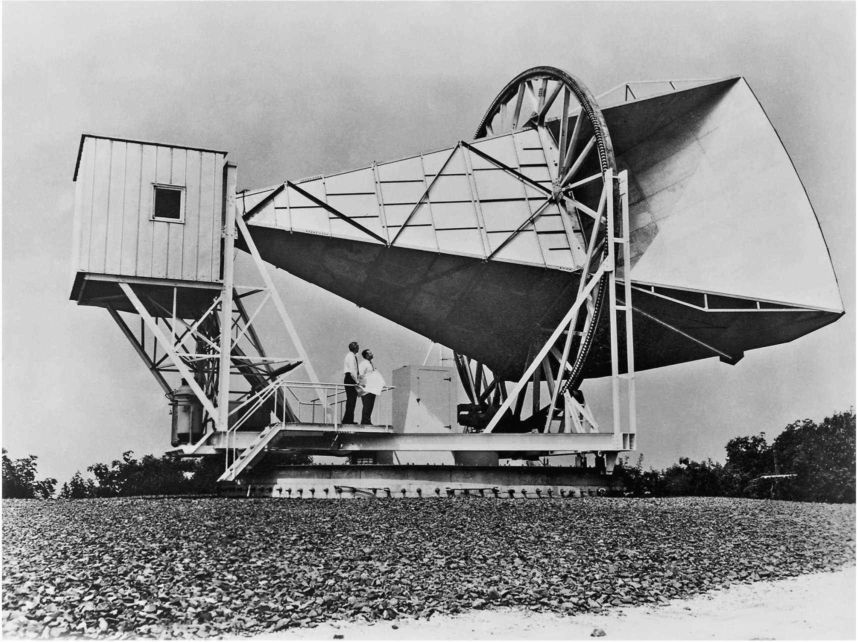

FIGURE 15 The 20-foot microwave horn antenna installed at the Bell Telephone Laboratories' Holmdel research facility. This is now designated as a US National Historical Landmark.

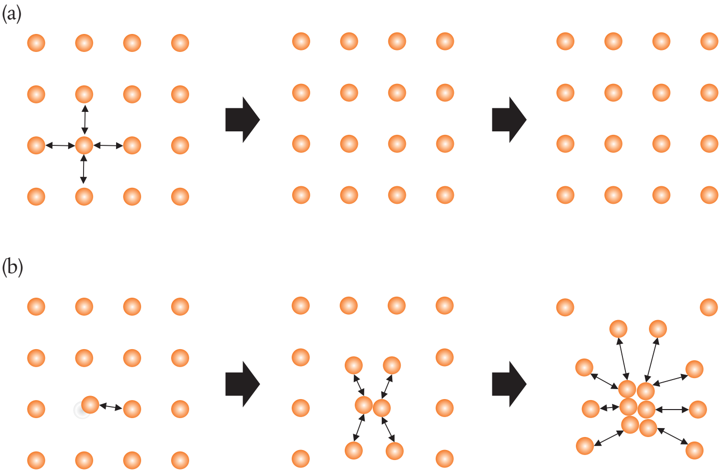

FIGURE 16 (a) In a perfectly uniform or isotropic distribution of matter, gravity acts equally in all directions and the matter remains frozen in place, even though spacetime itself might be expanding. In (b) we introduce a small anisotropy by displacing one of the balls slightly. Now the displaced ball feels a slightly stronger gravitational attraction to its nearest neighbour. Over time, the matter clumps together, forming a structure.

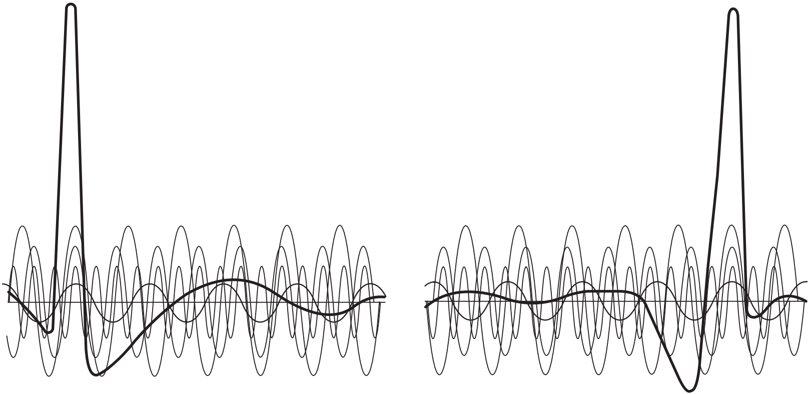

(a) (b)

FIGURE 17 Although waves are by definition delocalized, we can nevertheless add together lots of waves with different frequencies to create a superposition which produces a strong peak in one specific location in space, (a). This is called a 'wavepacket'. As the collection of waves moves, the peak moves along with it, giving the impression of a particle-like trajectory through space, (b).

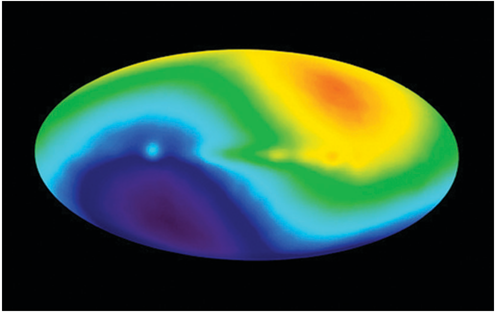

FIGURE 18 The motion of the Milky Way galaxy through the cosmic background radiation causes a small shift in measured temperatures, the radiation appearing a little hotter as we move towards it, a little cooler as we move away. This 'dipole variation' is shown in this false-colour, all-sky temperature map. Hotter regions (with a temperature a little over 0.003 kelvin higher than average) appear red, cooler regions (0.003 kelvin lower than average) appear blue. In this picture, the plane of the Milky Way galaxy lies horizontally along the centre.

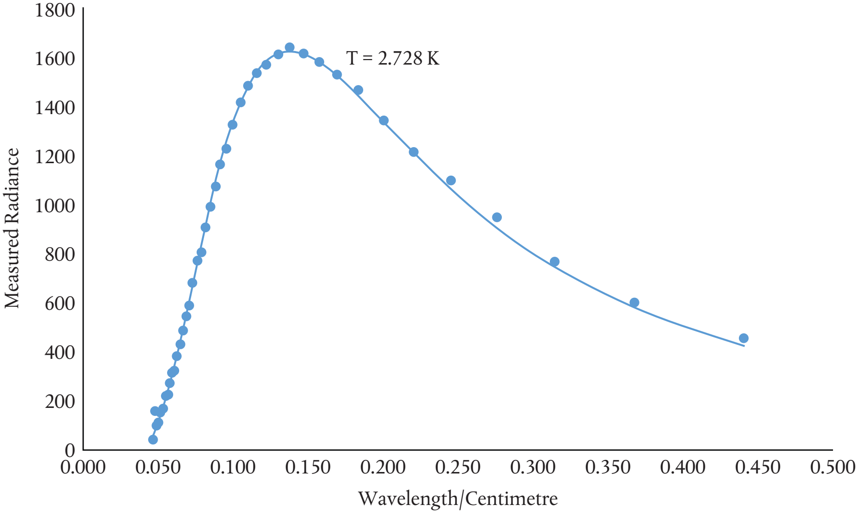

FIGURE 19 Measurements of the spectral radiance of the cosmic background radiation as a function of wavelength were reported by the COBE team in 1990. The spectrum is that of a black body with a temperature of 2.728 kelvin. The points represent the experimental measurements and the continuous line is the prediction based on a black-body spectrum. Adapted from D. J. Fixsen, E. S. Cheng, J. M. Gales, J. C. Mather, R. A. Shafer, and E. L. Wright, astro-ph/9605054, 10 May 1996.

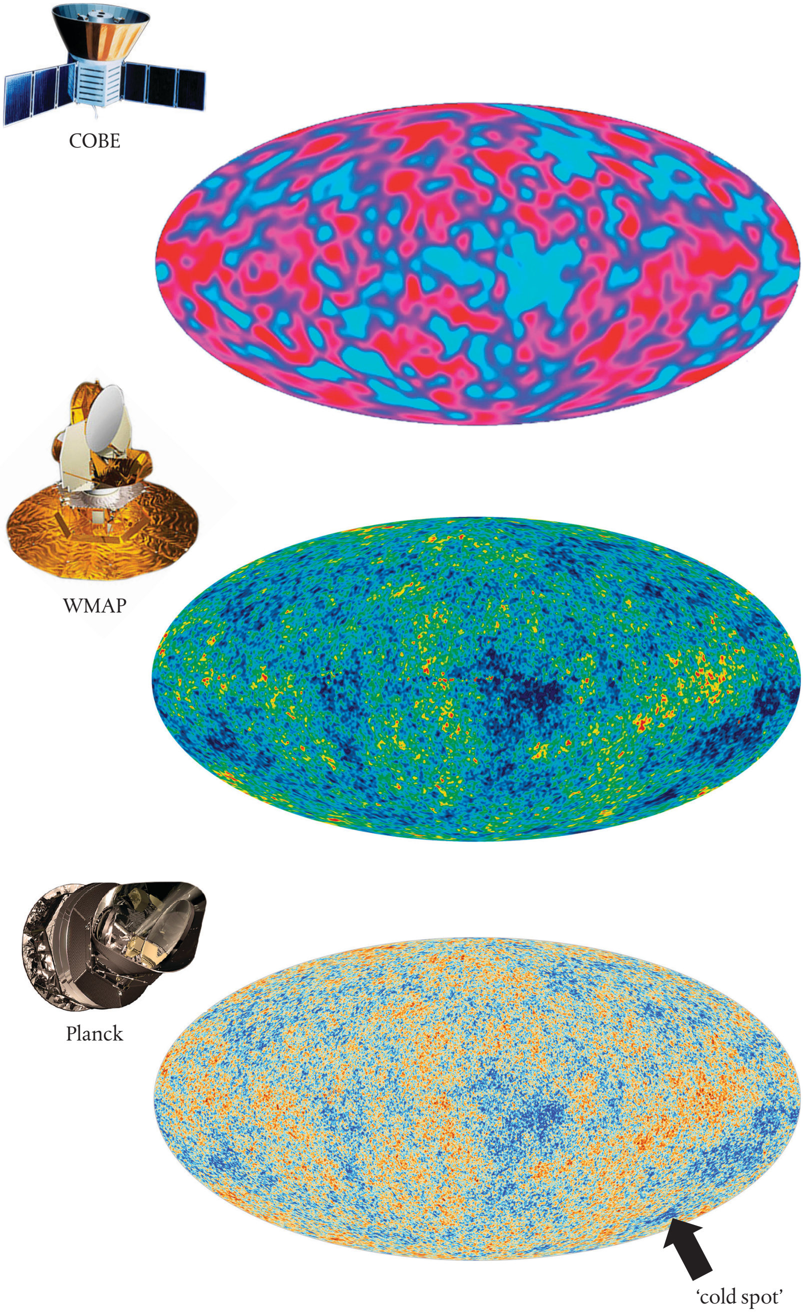

FIGURE 20 The detailed, all-sky map of temperature variations in the cosmic background radiation derived from data obtained from the COBE, WMAP (9-year results), and Planck satellites. The temperature variations are of the order of ±200 millionths of a degree and are shown as false-colour differences, with red indicating higher temperatures and blue indicating cooler temperatures. The angular resolution of this map has increased dramatically with successive missions.

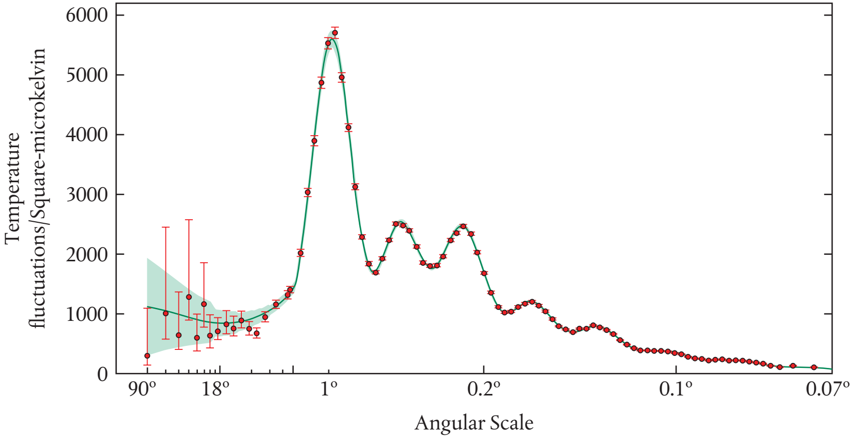

FIGURE 21 The variation of temperature fluctuations (measured in square microkelvin) with angular scale across the sky, derived from measurements of the cosmic background radiation by the Planck satellite. The Planck data are illustrated by the points with associated error bars and the best-fit Λ-CDM model prediction is shown as the continuous line.

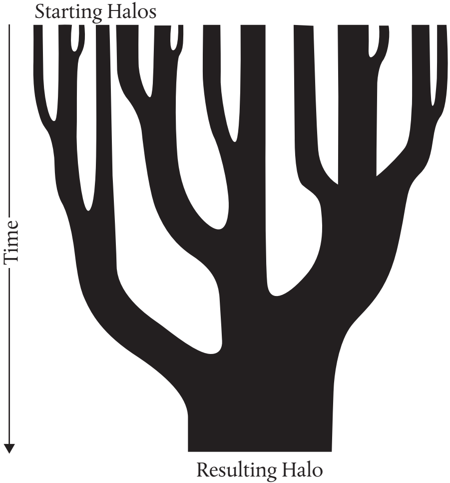

FIGURE 22 As dark matter halos form, they are attracted to other halos in their vicinity. The halos merge and coalesce, their history tracing the outlines of a 'merger tree' as illustrated here. As time passes, a single, large halo is formed. Adapted from Cedric Lacey and Shaun Cole, *Monthly Notices of the Royal Astronomical Society*, **262** (1993), p. 636.

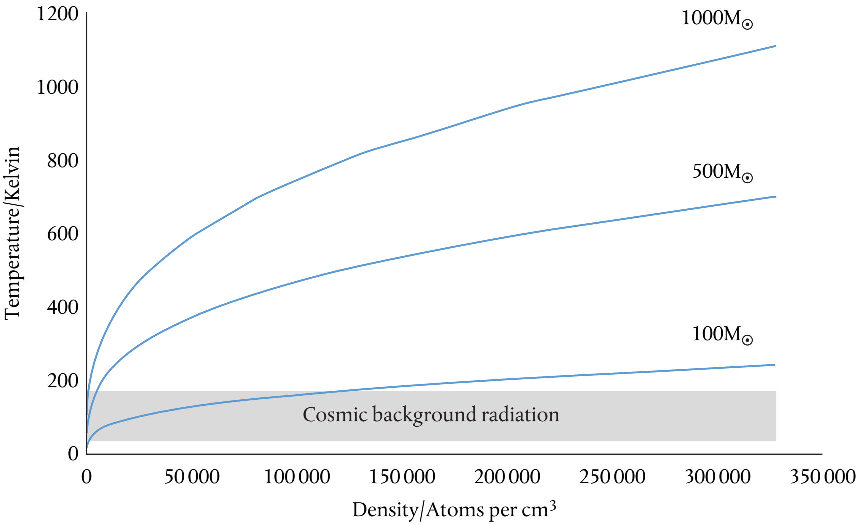

FIGURE 23 In 1902, British physicist James Jeans worked out the principles that determine whether or not a gas cloud will collapse to form a star. What will happen depends on the interplay between the cloud's mass, density, and temperature, as illustrated in these curves calculated for masses of hydrogen atoms of 100, 500, and 1000 $M_{\odot}$, where $M_{\odot}$ stands for the mass of the Sun. For a given mass and density, clouds with temperatures above the curve will not collapse, those with temperatures below the curve will collapse. The grey band indicates the temperature range of the cosmic background radiation 30–400 million years after the big bang. Under the conditions that prevailed in the early universe, the first stars are predicted to have had very large masses.

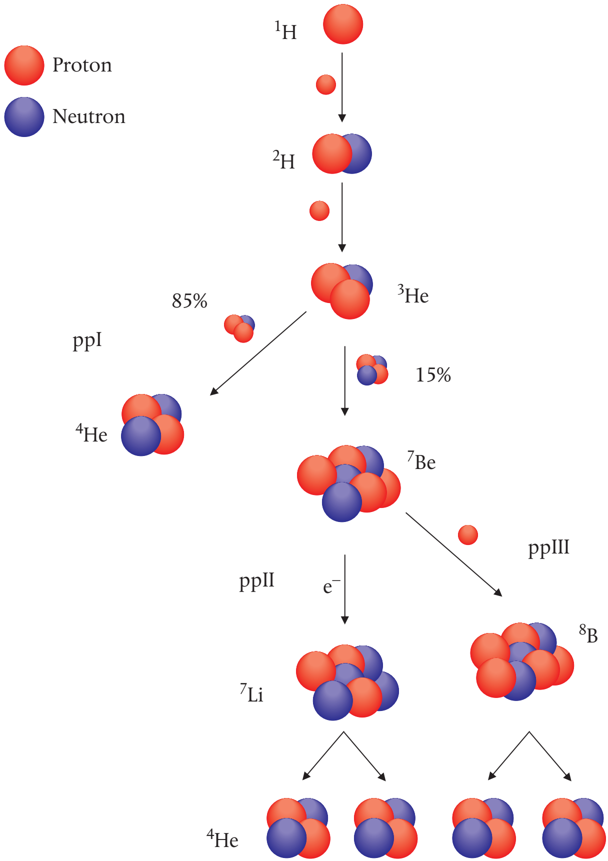

FIGURE 24 The chain of nuclear reactions involved in the initial stages of stellar nucleosynthesis is known as the proton-proton (p-p) chain.

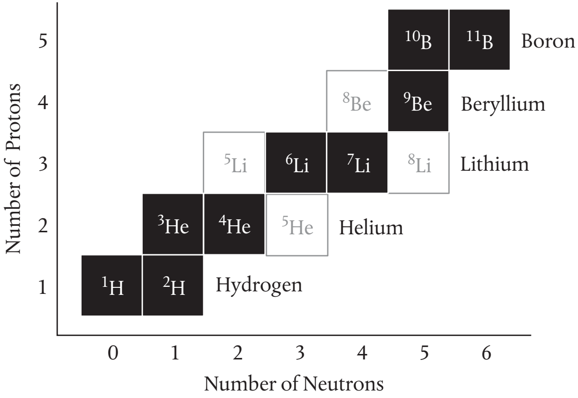

FIGURE 25 Adding single protons and neutrons to ^{1}H allows the building of a sequence of stable elements (black squares) up to ^{7}Li. But here we hit a bottleneck: there are no stable nuclei with eight nucleons. Adding a proton to ^{7}Li produces an unstable ^{8}Be nucleus, which decays very rapidly.

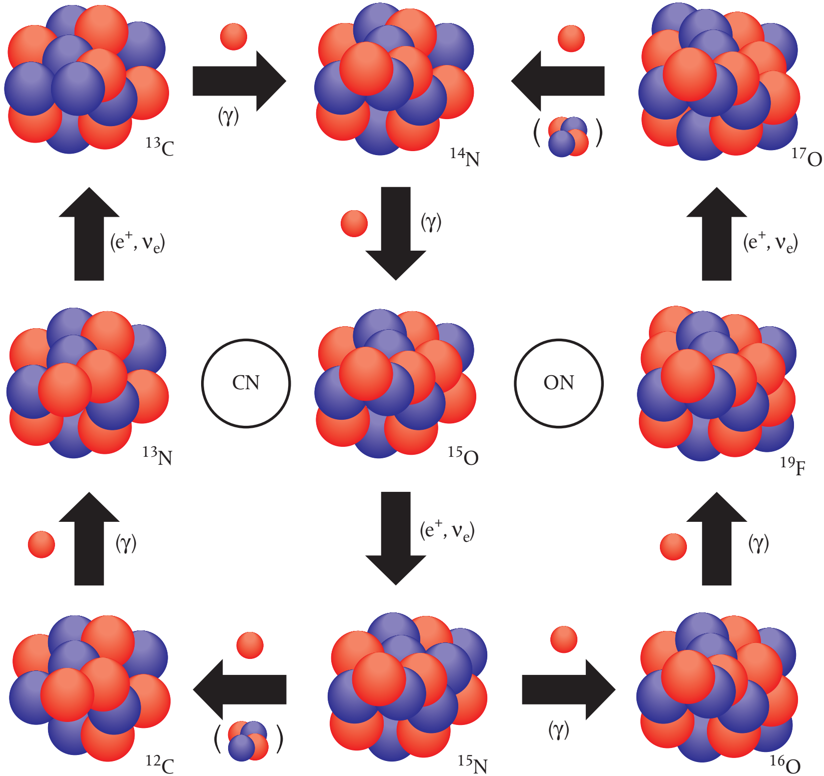

FIGURE 26 The CNO cycle. Isotopes of carbon, nitrogen, and oxygen form closed catalytic loops. Starting from the bottom left, a ^{12}C nucleus picks up a free proton to form ^{13}N, an isotope of nitrogen, emitting a high-energy photon (shown in brackets). This undergoes a weak-force decay, emitting a W^+ particle which transforms into a positron (e^+) and an electron neutrino (ν_e) to form ^{13}C. This picks up another proton to form ^{14}N, and another proton to form ^{15}O, an isotope of oxygen, which undergoes a weak force decay to ^{15}N. The CN cycle closes with a reaction involving the fusion of another proton and the emission of a ^{4}He nucleus (an alpha particle), bringing us back to ^{12}C. In this cycle, four protons have once again been combined to produce a helium nucleus. The ON cycle shown on the right does much the same job.

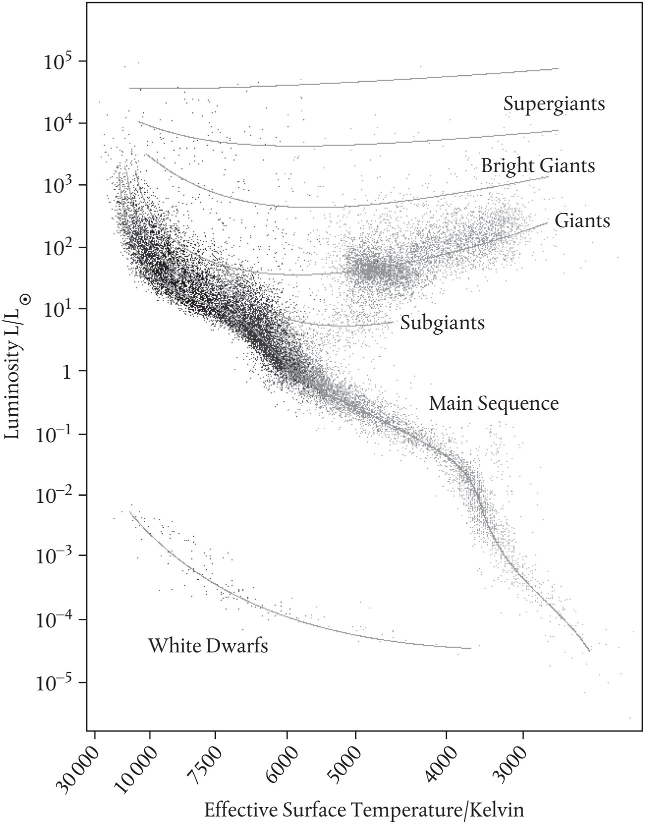

FIGURE 27 The Hertzsprung–Russell diagram maps the luminosity of stars (L, measured relative to the luminosity of the Sun, $L_{\odot}$) against their effective surface temperature. Most of the stars observed fall into a diagonal band called the main sequence. Stars in the main sequence are burning through their reserves of hydrogen. As the hydrogen is exhausted, the stars leave the main sequence to form red giants. Further evolution may result in the loss of mass through thermal pulsing, leaving White Dwarfs that no longer shine but glow through radiative cooling.

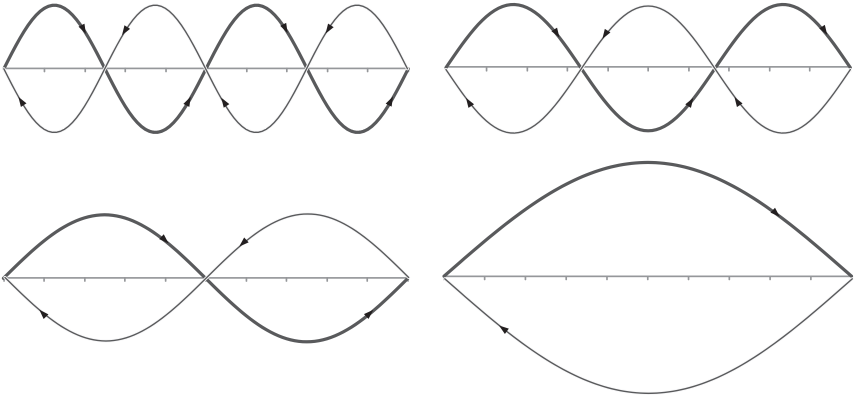

FIGURE 28 Examples of standing wave patterns. These are characterized by having zero height or amplitude at each end of the stopped string or length of pipe. The arrows give some sense of the direction in which the waves 'travel' although, once established, the waves appear to stand still.

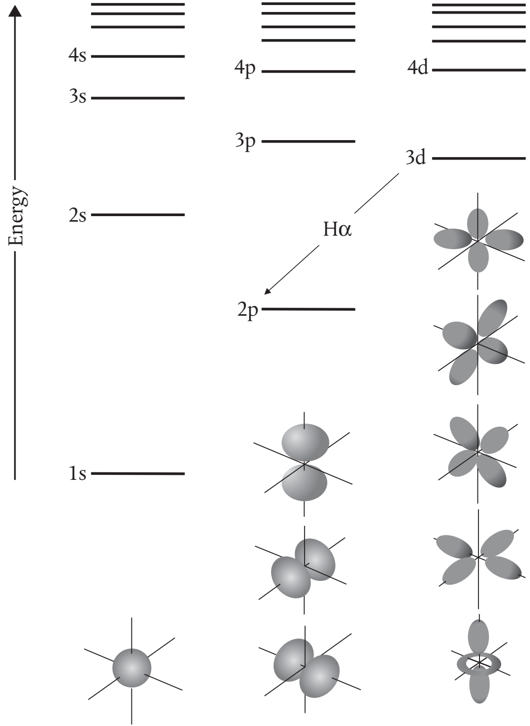

FIGURE 29 A selection of the lowest-energy hydrogen atomic orbitals. Each orbital represents a three-dimensional 'standing wave' pattern for the electron orbiting the nucleus. The lowest atomic energy levels are also shown. An electron in the 3d orbital will lose energy, falling to the 2p orbital, emitting red light with a wavelength of 656 nanometres. This produces a characteristic emission line called the Hα line.

(a)

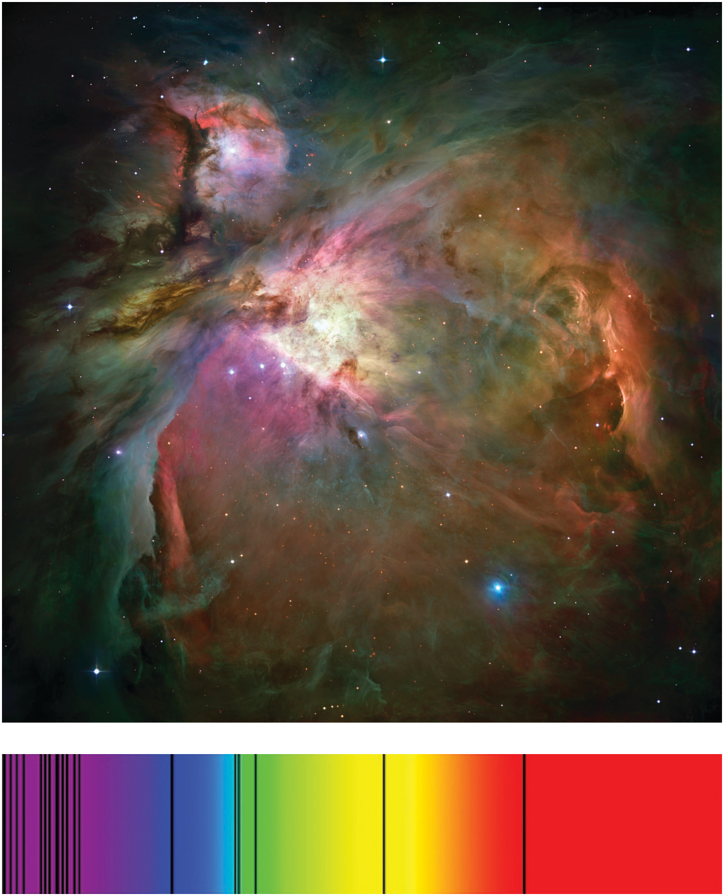

(b)

FIGURE 30 (a) Hα emission from hydrogen atoms lends a reddish hue to many true-colour photographs of nebulae, such as the Orion nebula. (b) If we pass sunlight through a prism, we will get the familiar rainbow pattern of colours in the visible spectrum. However, if we look closely, we may notice that this spectrum is crossed by a series of dark lines. These represent wavelengths of light that have been absorbed by atoms—including hydrogen atoms—in the outer layers of the Sun. This picture shows lines characteristic of hydrogen, including the Hα line in the red part of the spectrum.

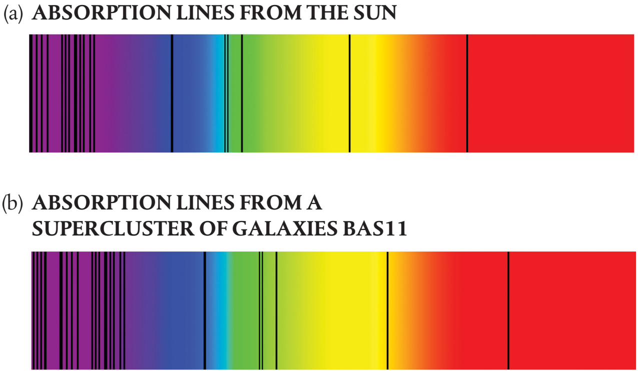

FIGURE 31 Atomic absorption lines crossing the spectrum of light from the Sun, (a), are shifted towards the red in light from a distant object which is moving away from us, (b). From the extent of the redshift, it is possible to work out the speed of the object.

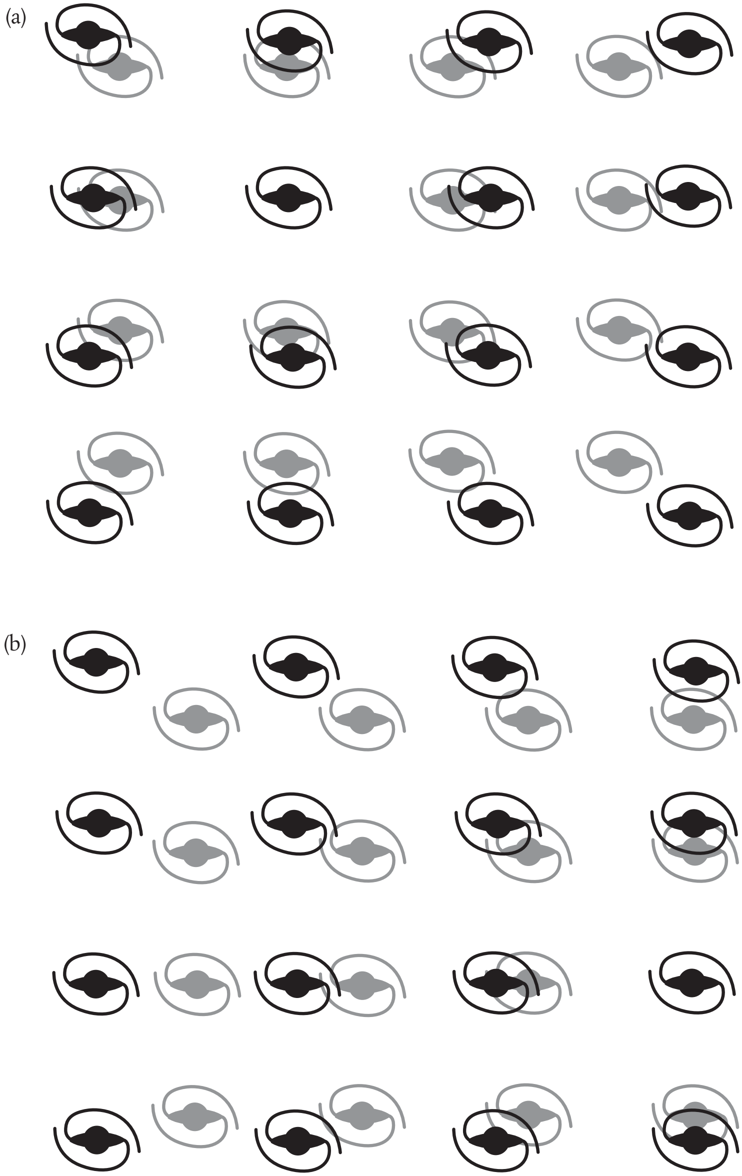

FIGURE 32 Imagine a universe consisting of a uniform distribution of galaxies. The pattern in grey represents this universe at some moment in time. The pattern in black is the distribution a short time later, after the universe has expanded. Let's now look at this from two different vantage points. From the perspective of the galaxy in row 2, column 2, shown in (a), all the galaxies around it have moved away, with more distant galaxies appearing to have moved the furthest. In (b), we fix on the galaxy in row 3, column 4. The result is the same—all the galaxies have moved away, with more distant galaxies moving the furthest. So the fact that we see most galaxies receding from us doesn't mean we're at the centre of the universe.

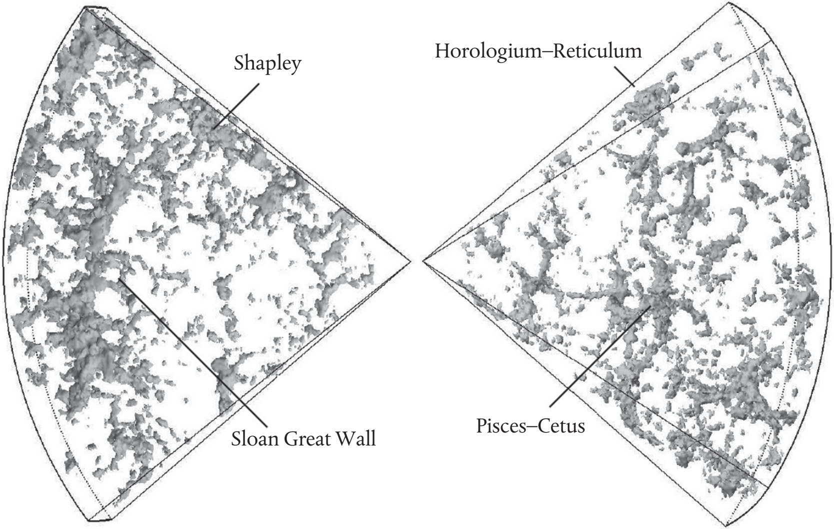

FIGURE 33 Sections of the map of galaxy redshift in the northern and southern hemispheres (relative to the plane of the Milky Way) measured in the 2dF Galaxy Redshift Survey. The map shows huge structures consisting of galaxy superclusters, among the largest known structures in the visible universe. The pattern of filaments, walls, and voids reflects the anisotropy in the distribution of matter in the early universe.

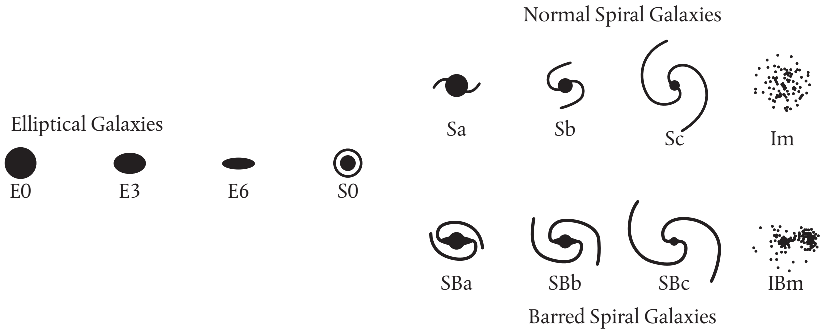

FIGURE 34 Hubble classified galaxies according to their shapes. Spiral galaxies are split into barred and normal spirals, with further subcategories of each (labelled a, b, and c) based on the density of stars in the central bulge and the tightness of the spiral arms. Elliptical galaxies are classified based on the dimensions of the ellipse. Further categories include the intermediate lenticular or S0 galaxies and the irregular galaxies. Adapted from R. G. Abraham, astro-ph/9809131 v1, 10 September 1998.

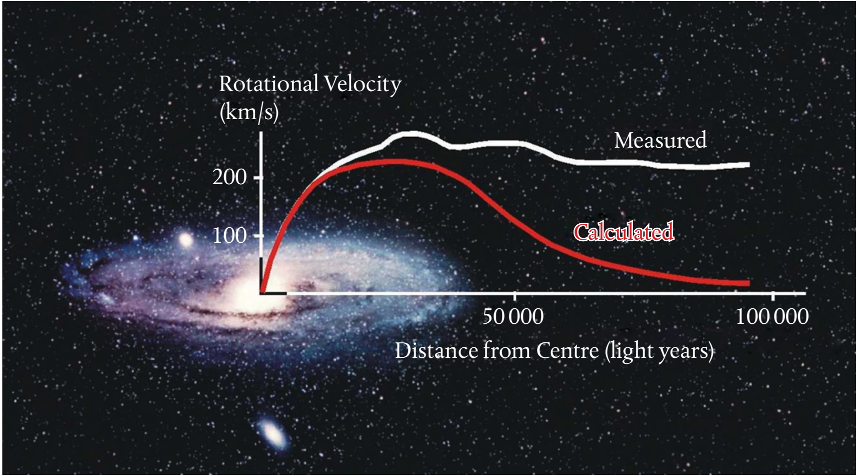

FIGURE 35 Simple Newtonian mechanics predicts that the stars in the Andromeda galaxy will orbit the centre with speeds that rise to a peak, before falling off with distance. However, the measured speeds flatten out with increasing distance. The measured behaviour is consistent with a dark matter halo that surrounds the galaxy.

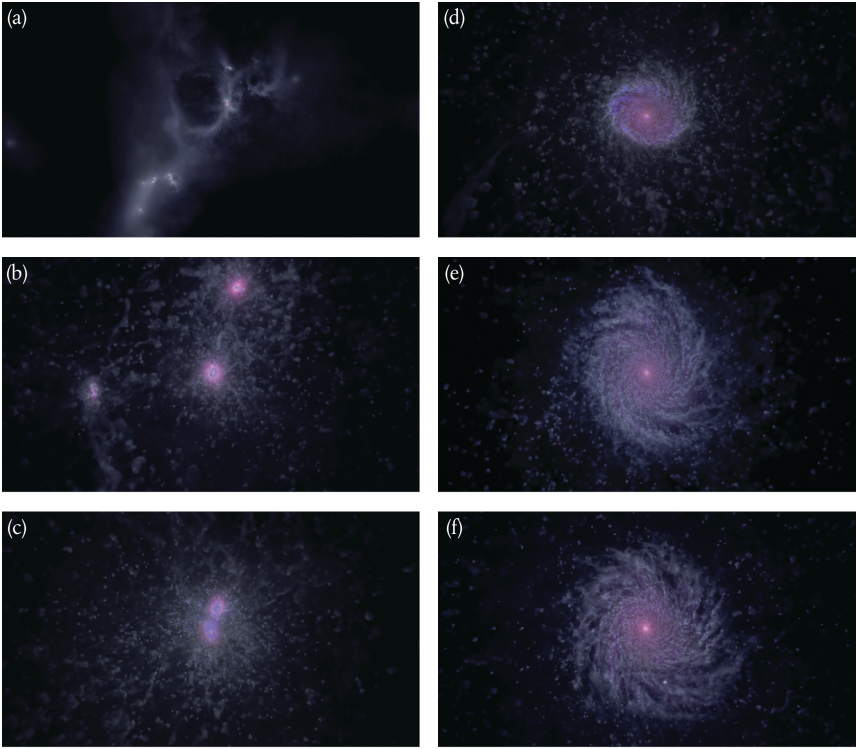

FIGURE 36 This computer simulation of the formation of a Milky Way type spiral galaxy shows the gradual accumulation of baryonic matter (mostly hydrogen and helium) within a large dark matter halo (a), about 500 million years after the big bang. Numerous proto-galaxies are formed which spin around, collide, and merge, (b). After about 4 billion years a single galaxy emerges with a well-defined centre, (c). A couple of billion years later the galaxy collides with another, (d), forming a larger galaxy which continues to accumulate baryonic gas and smaller satellite galaxies from its surroundings, (e). As we approach the present day, (f), the galaxy continues to evolve. These stills are taken from a movie of the simulation performed on the NASA Advanced Supercomputer by Fabio Governato and colleagues at the University of Washington.

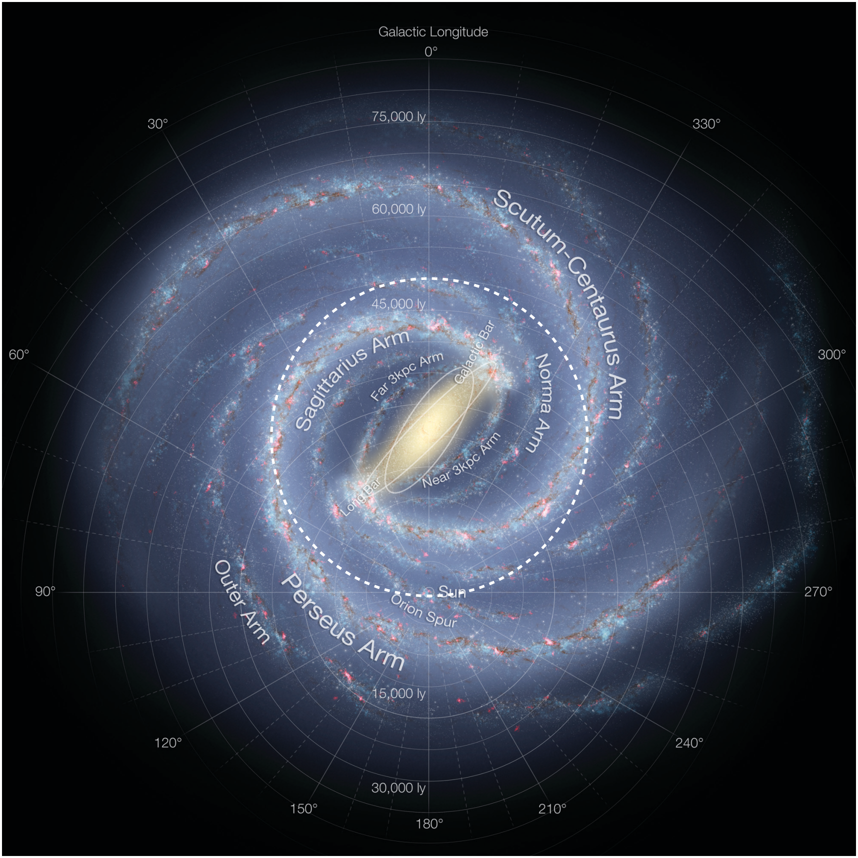

FIGURE 37 Artist's sketch of the Milky Way galaxy seen from above the galactic plane, based on data obtained at radio, infrared, and visible wavelengths. The Milky Way is believed to be a two-armed barred spiral with several secondary arms. The major arms are the Scutum-Centaurus Arm and Perseus Arm. The dashed circle has a radius of 27 000 light-years, and passes through the Orion Arm, which is where we will eventually find the Sun. Adapted from Ed Churchwell, Brian L. Babler, Marilyn R. Meade, Barbara A. Whitney, Robert Benjamin, Remy Indebetouw, *et al.*, *Publications of the Astronomical Society of the Pacific*, **121** (2009), p. 227.

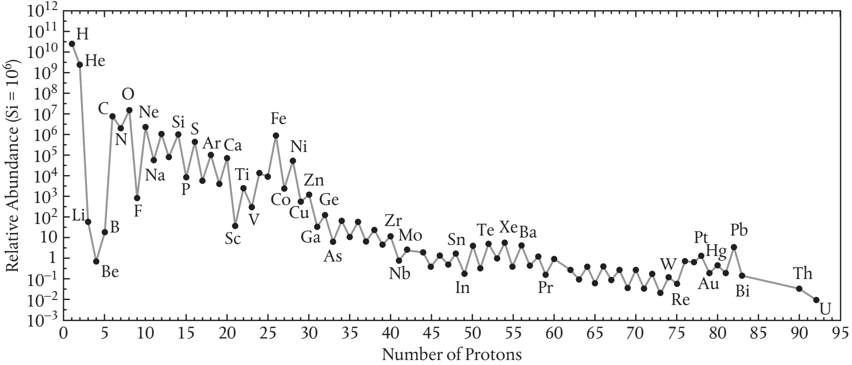

FIGURE 38 Abundances of chemical elements produced through primordial and stellar nucleosynthesis, in numbers of atoms per million relative to silicon. These abundances refer to our own Sun, and there is evidence to suggest that element abundances in newly formed giant molecular clouds may be a little different, but we can presume that by the time the cloud was ready to give birth to the Sun it possessed a pattern of abundances not much different from that shown here. Note the logarithmic abundance scale.

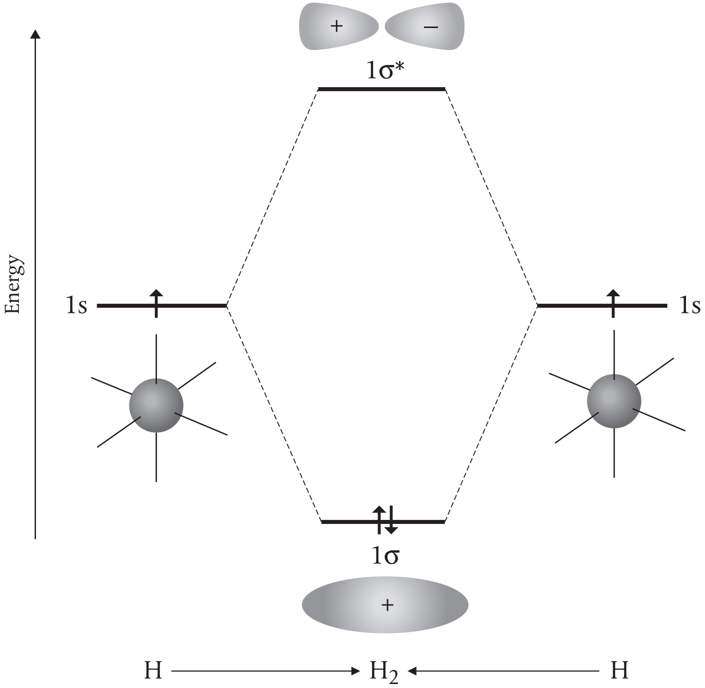

FIGURE 39 Overlap of the 1s electron orbitals from two hydrogen atoms produces a lower-energy 'constructive' bonding orbital (1σ) and a 'destructive' anti-bonding orbital (1σ*). The two electrons can now both occupy the bonding orbital, provided that their spins are paired. The result is a hydrogen molecule in which the two electrons form a single bond.

TABLE 2: Illustrative examples of interstellar molecules

Number of atoms	Examples
2	molecular hydrogen (H_2), carbon monoxide (CO), molecular nitrogen (N_2), molecular oxygen (O_2), sodium chloride (NaCl), iron oxide (FeO), hydrogen chloride (HCl), hydrogen fluoride (HF), carborundum (SiC), titanium oxide (TiO)
3	carbon dioxide (CO_2), water (H_2O), hydrogen sulphide (H_2S), hydrogen cyanide (HCN), potassium cyanide (KCN), nitrous oxide (N_2O), sodium hydroxide (NaOH), ozone (O_3), sulphur dioxide (SO_2), titanium dioxide (TiO_2)
4	acetylene (C_2H_2), formaldehyde (H_2CO), hydrogen peroxide (H_2O_2), ammonia (NH_3), isocyanic acid (HNCO)
5	methane (CH_4), ketene (H_2C_2O), cyanoacetylene (HC_3N), formic acid (HCO_2H), ammonium ion (NH_4^+)
6	ethylene (C_2H_4), acetonitrile (CH_3CN), methanol (CH_3OH)
7	methylamine (CH_3NH_2), acrylonitrile (CH_2CHCN), ethylene oxide (c-C_2H_4O)*, vinylalcohol (CH_2CHOH), acetaldehyde (CH_3CHO)
8	acetic acid (CH_3CO_2H), glycoaldehyde (CH_2OHCHO), methylcyanoacetylene (CH_3C_3N)
9	dimethylether (CH_3OCH_3), ethylalcohol (C_2H_5OH), propylene (CH_3CHCH_2)
10	acetone ($(CH_3)_2CO$), glycine ($NH_2CH_2CO_2H$), ethylene glycol ($(CH_2OH)_2$)
>10	methylacetate ($CH_3CO_2CH_3$), benzene (C_6H_6), cyanopentaacetylene ($HC_{11}N$), anthracene ($C_{14}H_{10}$), pyrene ($C_{16}H_{10}$), buckminsterfullerene (C_{60}), 70-fullerene (C_{70})

*The prefix *c*- indicates a cyclic molecule.

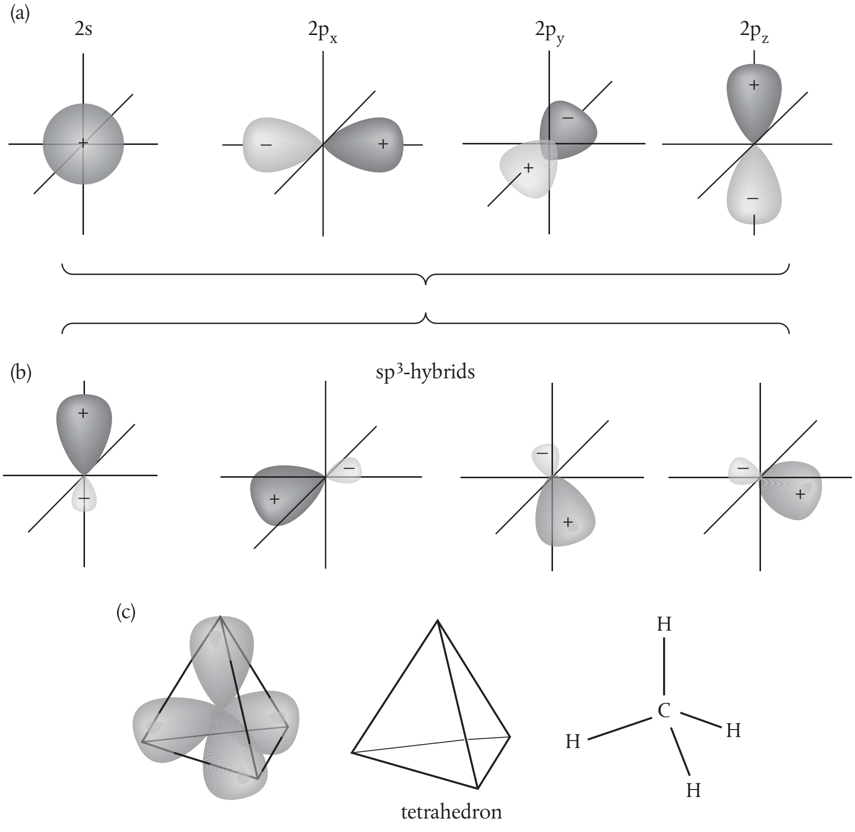

FIGURE 40 The central carbon atom in methane has two electrons in a 2s orbital and two electrons in each of two 2p orbitals, leaving the third 2p orbital vacant. But if one of the 2s electrons is promoted into the vacant 2p orbital, it is possible to mix all four of these together, (a). The result is four identical sp^3-hybrid orbitals, (b). The sp^3-hybrid orbitals produce a tetrahedral shape, (c).

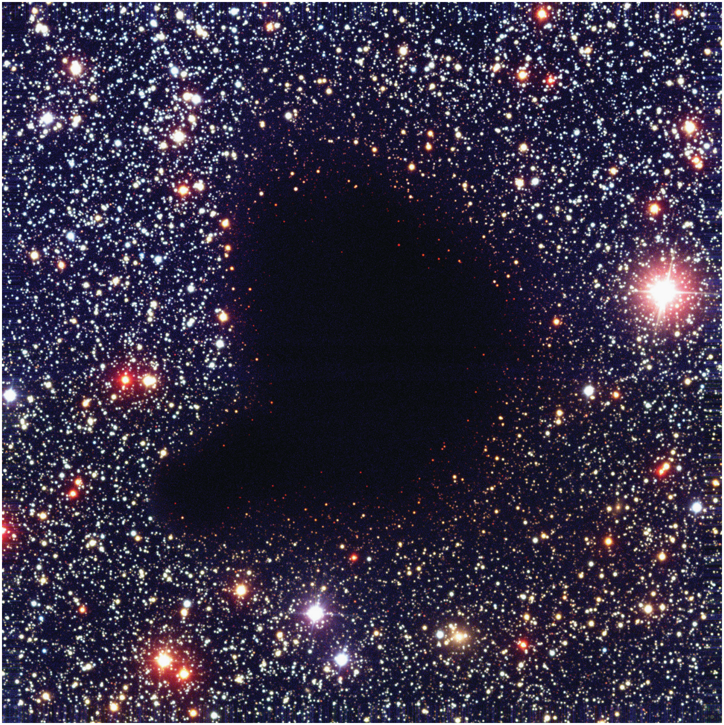

FIGURE 41 Barnard 68 is a molecular cloud in the constellation Ophiuchus with a mass of about 3 $M_\odot$ measuring about half a light-year in diameter. This is a composite of visible and near-infrared images obtained in 1999 and shows that the light from more distant stars in the Milky Way is completely obscured by dust particles in the cloud.

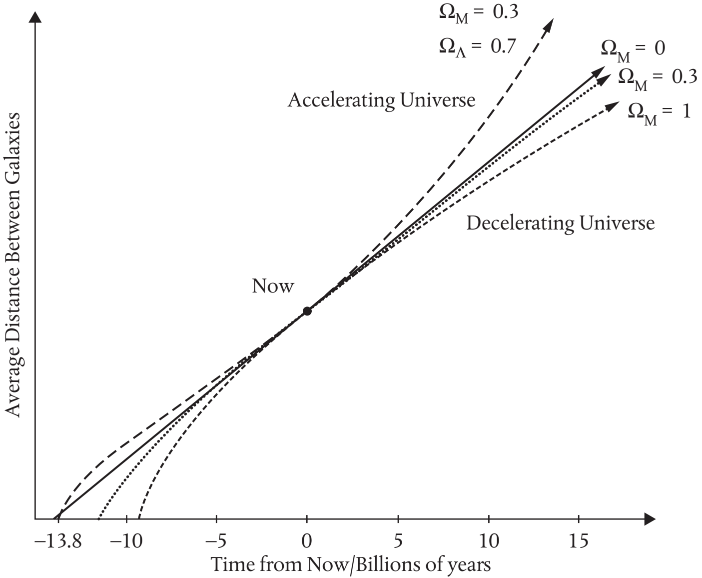

FIGURE 42 The future evolution of the universe depends on the density parameter Ω, which may be comprised of contributions from the density of matter (Ω_M) and the density of dark energy (Ω_Λ).

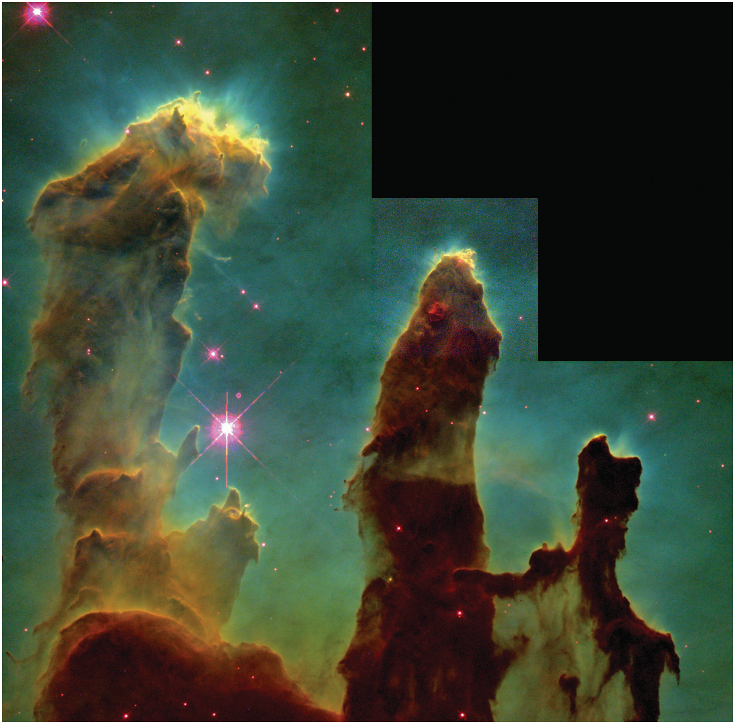

FIGURE 43 The 'Pillars of Creation', huge columns of molecular hydrogen and dust grains in the Eagle Nebula in the constellation Serpens. These columns are several light-years in length. This false-colour picture is a composite of 32 images taken using four different cameras mounted on the Hubble Space Telescope. The colours correspond to emission from different atomic and ionic constituents in the cloud: green for hydrogen atoms, red for singly charged sulphur (S^+) ions, and blue for oxygen (O^{2+}) ions.

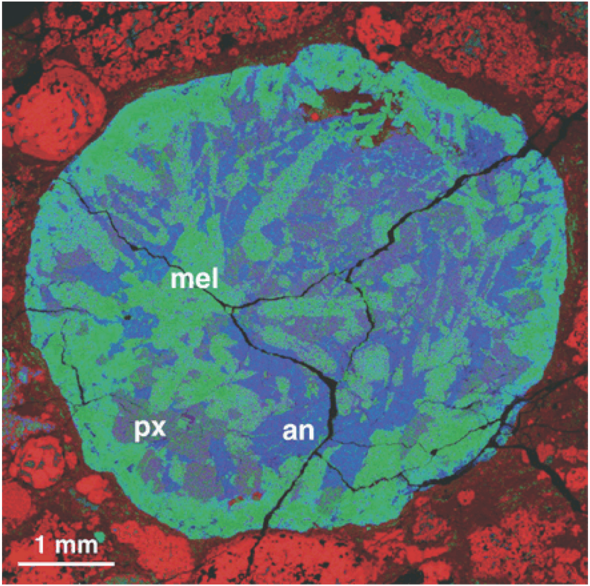

FIGURE 44 X-ray picture of a calcium-aluminium-rich inclusion in the Efremovka meteorite which, like Allende, is a carbonaceous chondrite. The picture shows different phases in the rock corresponding to different mineral structures, such as melilite (mel), pyroxene (px), and anorthite (an). The false colours reflect the elemental composition: calcium is green, aluminium is blue and magnesium is red. Adapted from: Ernst Zinner, *Science*, **300** (2003), pp. 265–7.

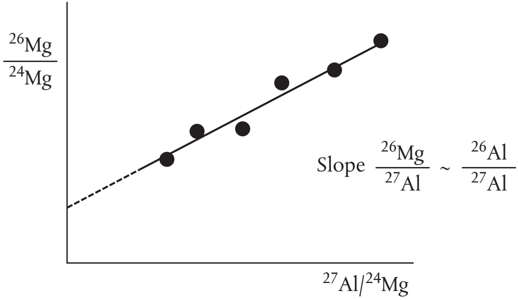

FIGURE 45 A plot of $^{26}Mg/^{24}Mg$ vs $^{27}Al/^{24}Mg$ for different minerals within a calcium-aluminium-rich inclusion can be used to infer an excess of the short-lived isotope ^{26}Al in the early stages of the formation of the Sun and solar system. The slope of this plot is related to the ratio $^{26}Mg/^{27}Al$. Any excess ^{26}Mg must be derived from the decay of ^{26}Al, so the magnitude of the slope also indicates an excess of ^{26}Al vs the stable isotope ^{27}Al.

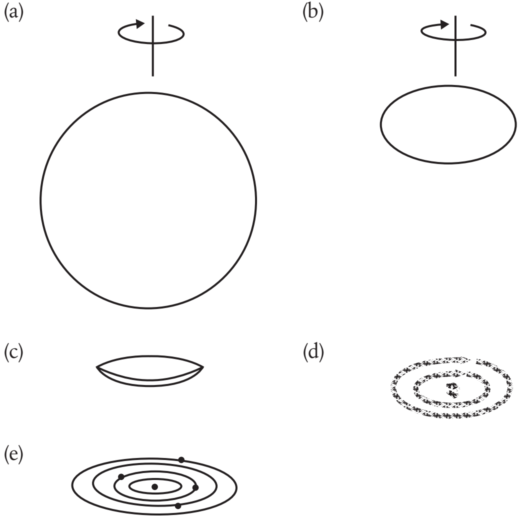

FIGURE 46 In the version of the nebular hypothesis due to Kant and Laplace, the formation of the solar system is initiated by the collapse of a near-spherical rotating cloud of gas and dust (a). As the cloud collapses it spins faster and starts to flatten (b), eventually forming a lenticular shape, like a lens (c). As the core collapses further to form the Sun, material in the flattened disk gathers together to form annular rings (d). These rings eventually condense to form the planets (e). Adapted from M. M. Woolfson, *Quarterly Journal of the Royal Astronomical Society*, **34** (1993), p. 2.

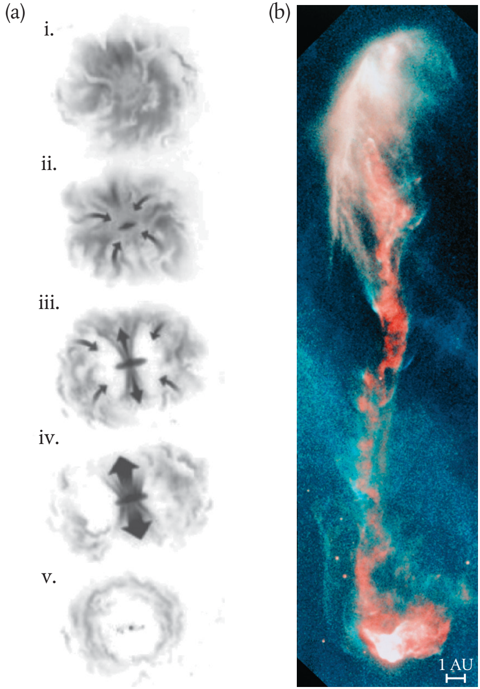

FIGURE 47 The diagram on the left shows the various stages in proto-stellar evolution, starting with a giant molecular cloud (i). The collapse of gas and dust within the cloud forms a rotating core (ii). As the core contracts it reduces its angular momentum by emitting jets of gas from its poles, called bipolar outflows (iii). The ejected gas forms an elongated nebula, called a Herbig–Haro Object, such as HH47 shown on the right in a photograph taken by the Hubble Space Telescope (the scale bar to the bottom right indicates 1 astronomical unit (AU), equal to the average distance from the Earth to the Sun, about 150 million kilometres). As the protostar matures to the T Tauri phase, convection currents produce strong winds which clear away volatile material from the protostar's accretion disk and outer cloud (iv). The protostar becomes visible, and follows the Hayashi track on its way to becoming a main sequence star (v). The diagram on the left is adapted from William H. Waller, *The Milky Way: An Insider's Guide*, Princeton University Press, 2013.

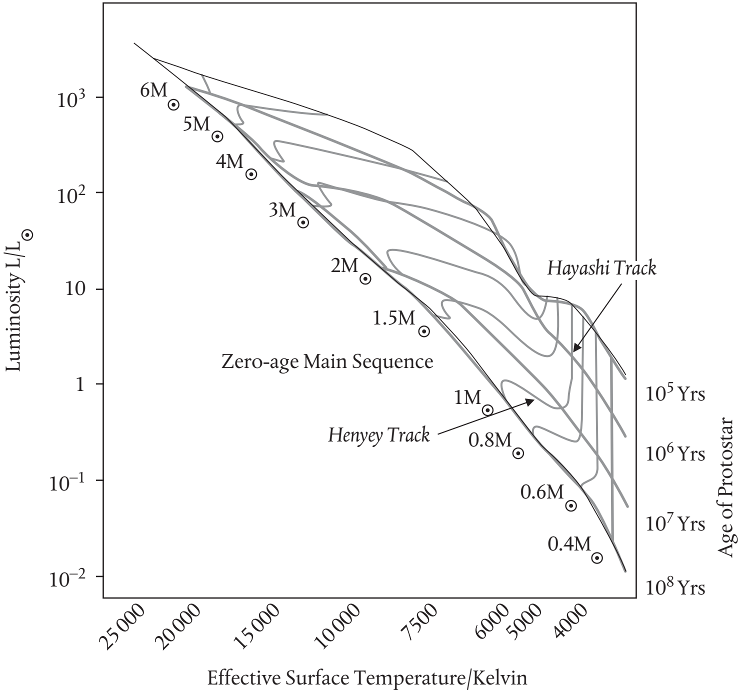

FIGURE 48 The evolution of young stellar objects is determined by the physical relationships established between mass, density, core temperature, opacity, temperature differentials, and convection. This figure shows Hayashi–Henyey trails for a range of stellar masses. The larger the mass, the faster the protostar evolves.

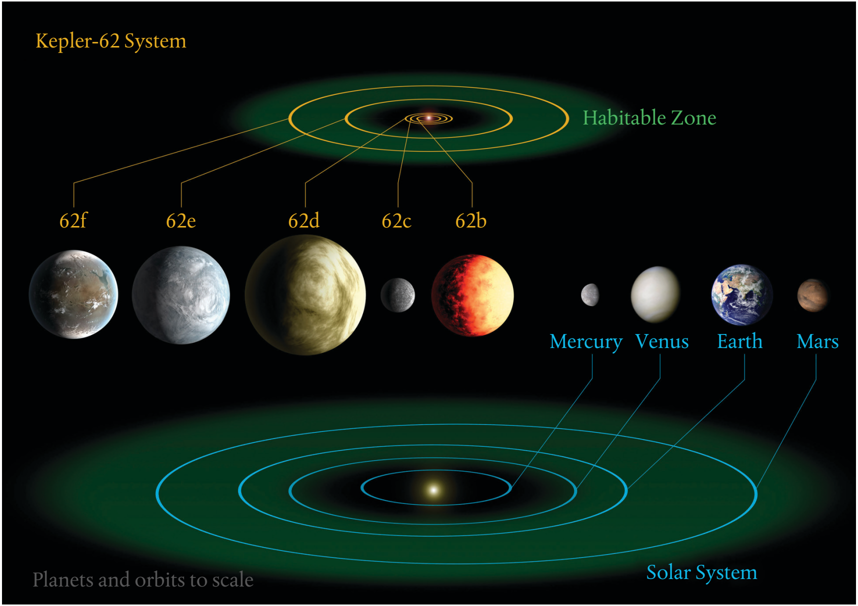

FIGURE 49 Artist's impression of the exoplanetary system of Kepler-62 and a comparison with the terrestrial planets of the inner solar system. The exoplanets Kepler-62e and -62f are 'super-Earths', with radii 1.61 and 1.41 times that of Earth, orbiting in the system's 'habitable zone' with orbital periods of 122 and 267 days, respectively. Both sets of planets are drawn to scale.

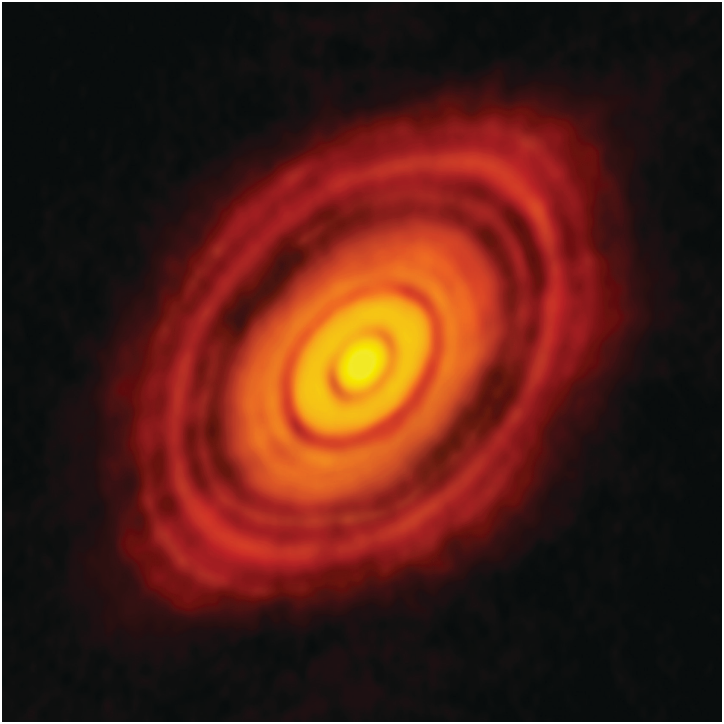

FIGURE 50 In this image from the ALMA observatory in Chile, the protoplanetary disk surrounding the young star HL Tauri can be clearly seen in the form of a series of concentric rings separated by voids. HL Tau lies about 450 light-years from Earth in the constellation Taurus, in the Taurus Molecular Cloud.

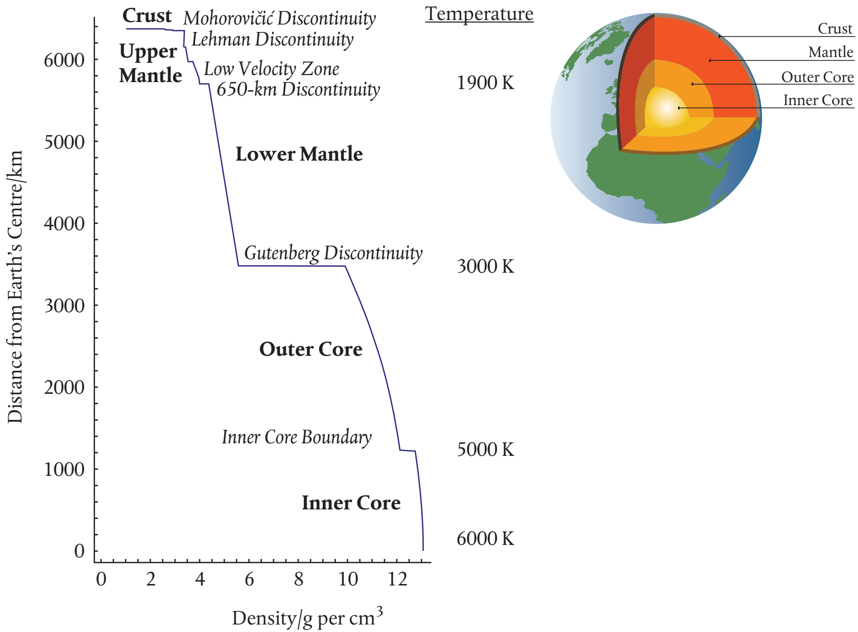

FIGURE 51 The density of material from which the Earth is composed increases with depth. The boundaries between each layer are marked by abrupt changes in density which can be detected in the patterns and timings of shockwaves from earthquakes recorded by seismometers. The inset shows the distribution of inner and outer core, mantle, and crust.

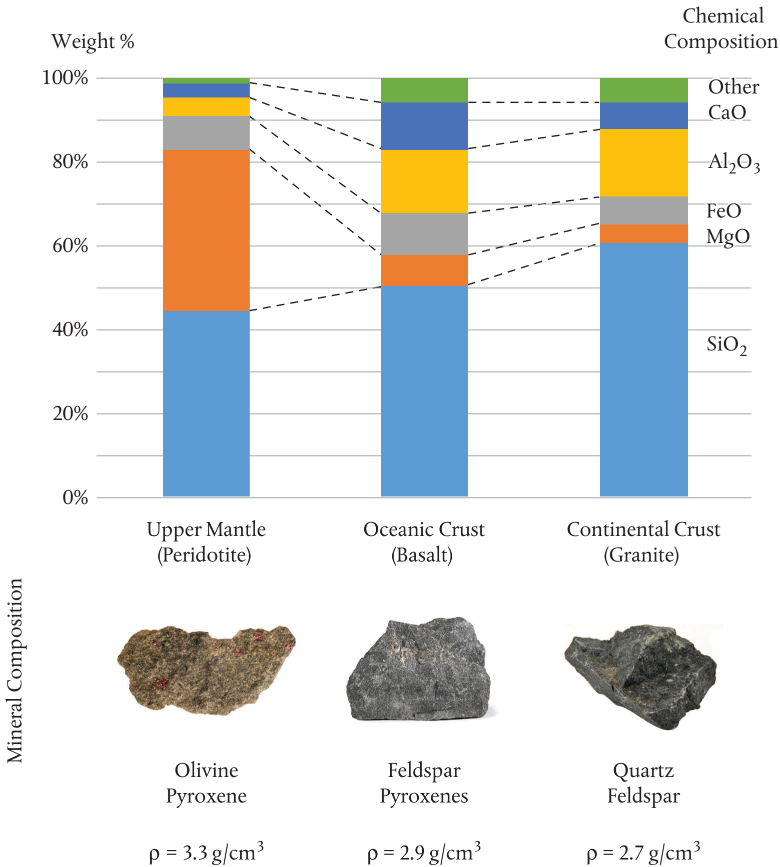

FIGURE 52 The upper mantle, oceanic crust, and continental crust are composed largely of three rock types, peridotite, basalt, and granite. These rocks have different mineral compositions, with the principal mineral types shown here. But these are complex mixtures of complex chemicals, and to get a sense of what happens it helps to look at the changes in chemical composition. The bar charts show the proportion (in weight per cent) of five oxides for each rock type. As these proportions change, the density (ρ) of the rock declines.

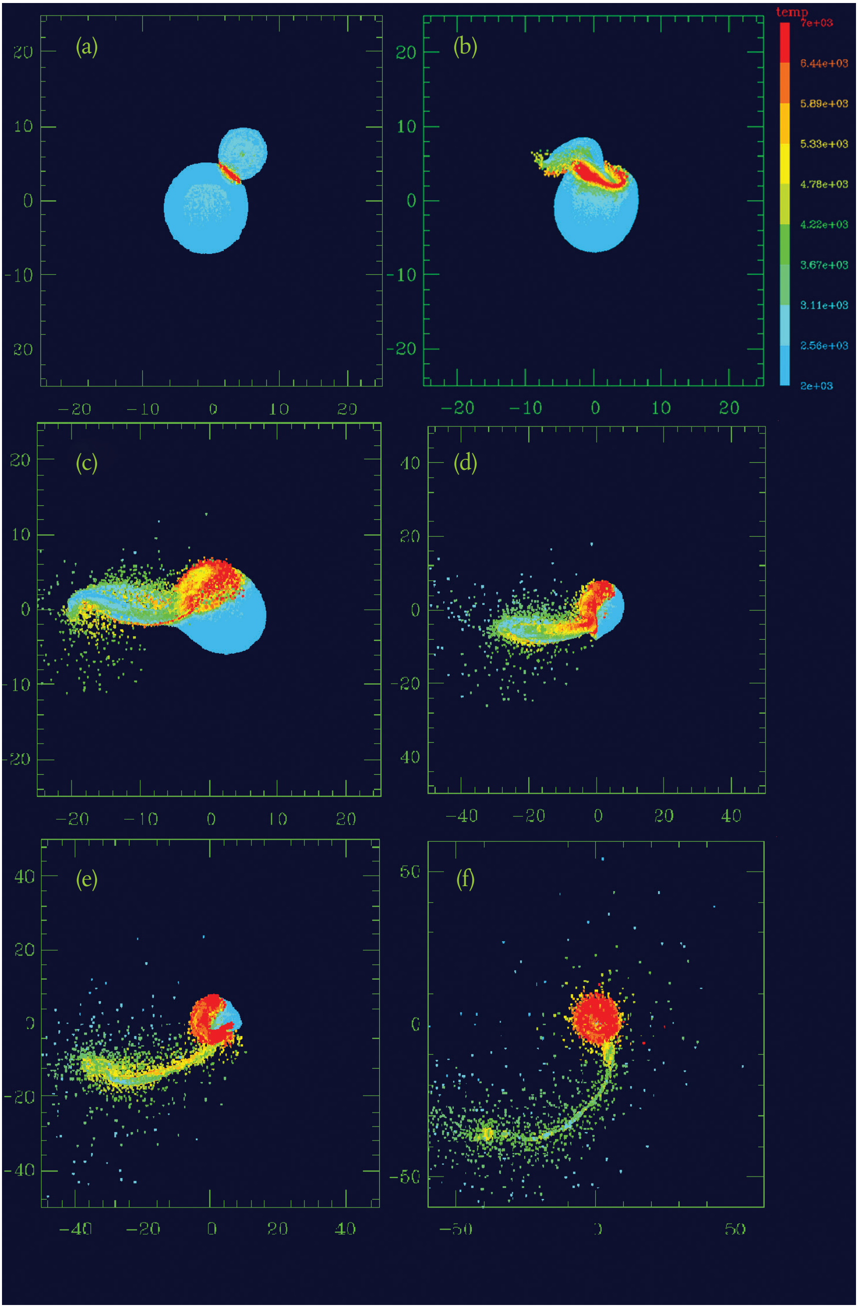

FIGURE 53 Computer simulations of a moon-forming impact reported in 2004 by planetary scientist Robin M. Canup at the Southwest Research Institute in Boulder, Colorado. These 'snapshots' show the unfolding collision and its effects at different times following the impact. (a) 6.5 minutes; (b) 19.4 minutes; (c) 51.8 minutes; (d) 84.1 minutes; (e) 129.4 minutes; and (f) 291.1 minutes. Note the change of distance scale (in thousands of kilometres) between frames (c) and (d) and (e) and (f). Temperatures are colour-coded from 2000 to 7000 kelvin. Adapted with permission from Robin M. Canup, *Icarus*, **168** (2004), p. 433.

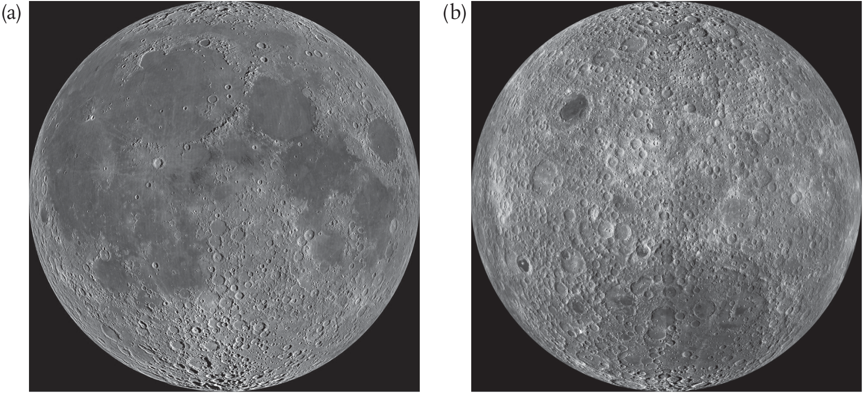

FIGURE 54 The familiar near side of the Moon (a) has lunar *maria,* or 'seas', which appear as dark patches of the surface, and lunar *highlands* which are lighter. In contrast the surface of the far side of the Moon (b) features only highlands and has a much thicker crust.

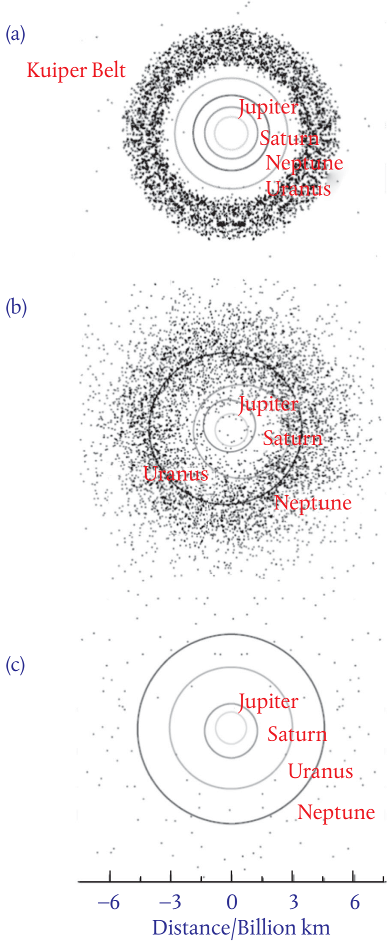

FIGURE 55 Computer simulations of planetary migration in the outer solar system demonstrate a connection with a period of intense cometary activity called the Late Heavy Bombardment. In (a) the outer planets line up in their initial sequence, Jupiter, Saturn, Neptune, and Uranus, surrounded by a thick band of planetesimals called the Kuiper belt. In (b), Jupiter and Saturn enter a 2:1 orbital resonance. Neptune is pushed out of its orbit by Saturn and is hurled into the Kuiper belt, dislodging planetesimals which are caught by the Sun's gravity and dragged in towards the inner planets (not shown in this figure). Jupiter is pushed closer to the asteroid belt, dislodging more planetesimals. The result is seen in (c), which shows the outer planets now in the 'right' order, and a greatly diluted Kuiper belt. Adapted from R. Gomes, H. F. Levison, K. Tsiganis, and A. Morbidelli, *Nature*, **435** (2005), p. 466.

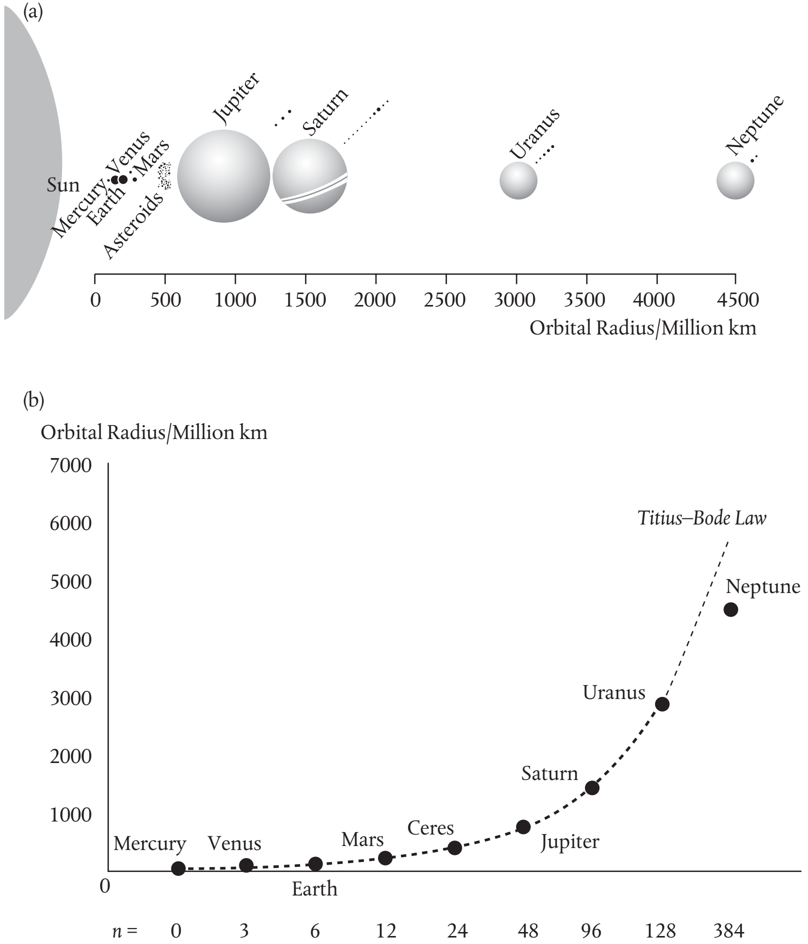

FIGURE 56 Following planetary migration and the Late Heavy Bombardment, 700 million years after the solar system was first formed, the planets take up the orbits that are familiar to us today. These are shown in (a), with the planets drawn to scale (though not consistent with the linear distance scale used to show the orbital radii). In (b), the planetary orbits (black circles) are compared with the predictions of the Titius–Bode law (dashed line).

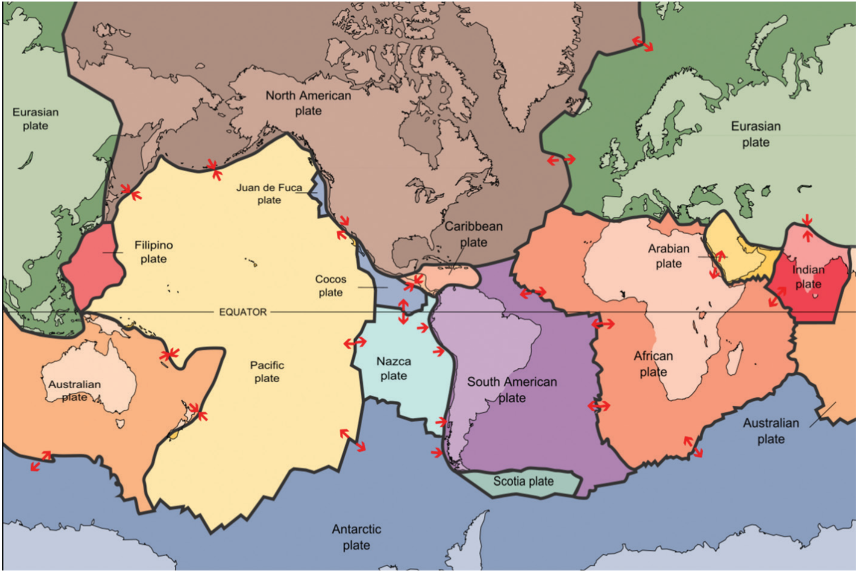

FIGURE 57 The Earth's uppermost mantle and crust (collectively called the lithosphere) breaks up to form a series of tectonic plates which move around the surface. This figure shows the plates as they appear today. 'Divergent' plate boundaries are illustrated by arrows pulling in opposite directions (←→). These appear in the middle of the oceans, the two most prominent being the Mid-Atlantic Ridge and the East Pacific Rise. Note that these divergent plate boundaries tend to run north to south, suggesting an intimate relationship with the Earth's rotation. Along these boundaries the seafloor spreads, renewing the crust with fresh material. At a 'convergent' boundary (→←) the crust of one plate is sucked down into the upper mantle, thrusting the crust of the other plate upwards to form a mountain range.

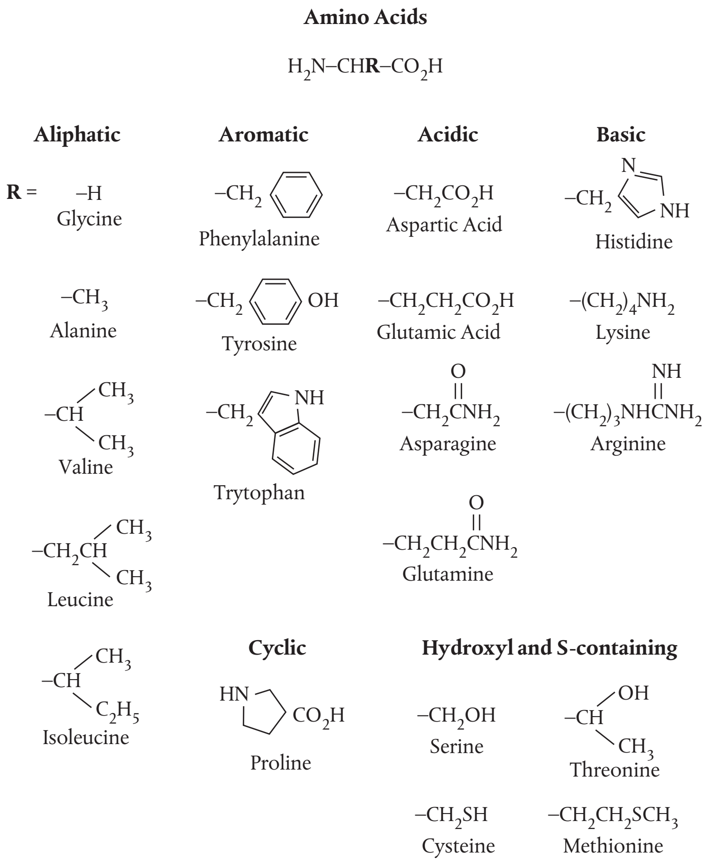

FIGURE 58 The core 20 amino acids involved in biochemical systems, organized according to the nature of their chemical structures. Most (19 of 20) conform to the general formula given at the top, the exception being the cyclic amino acid proline. See endnote 4 for an explanation of the cyclic structures which feature in proline, phenylalanine, tyrosine, tryptophan, and histidine.

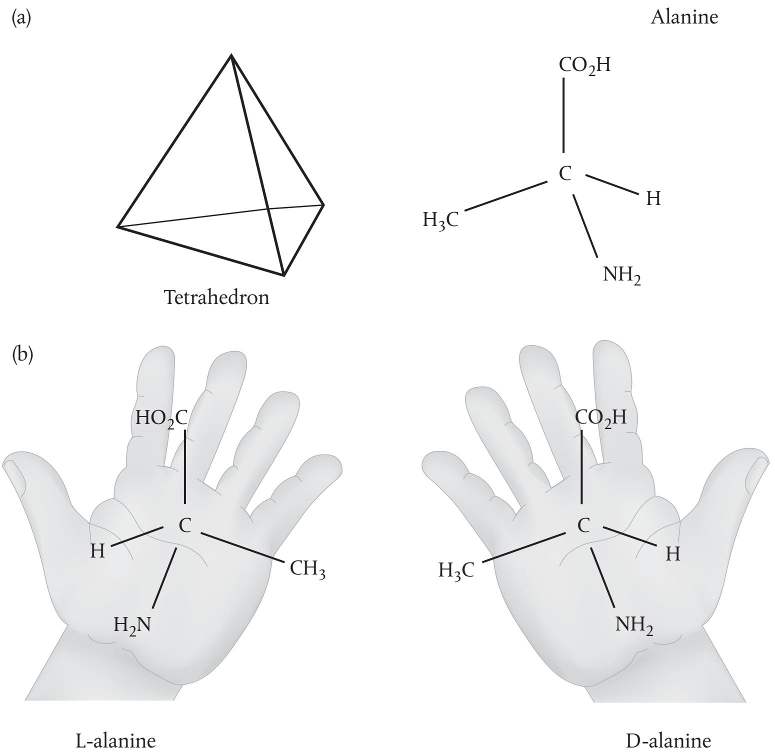

FIGURE 59 The amino acid alanine has four different atoms or functional groups bonded to the central carbon atom, each of which takes up a place at the apex of a tetrahedron (a). There are two different ways of distributing these groups, which represent mirror image forms (b). Such molecules are said to be chiral, and the different forms are called enantiomers.

Nucleotides

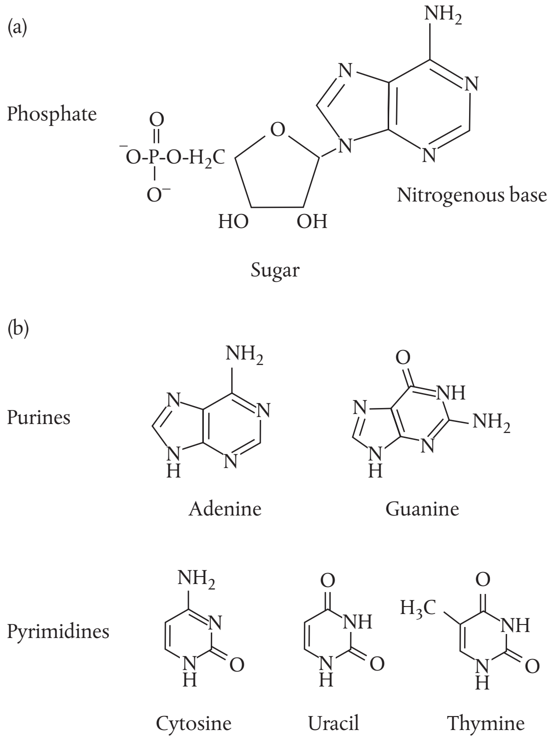

FIGURE 60 Nucleotides are the building blocks of RNA and DNA. They consist of a pentagonal ribose (or deoxyribose) sugar unit, a phosphate unit with one, two, or three phosphate groups, and a nitrogenous base (a). The bases are purines (adenine, guanine) or pyrimidines (cytosine, uracil, and thymine), shown in (b). The nucleotide shown in (a) possesses an adenine base unit and a single phosphate group and is called adenosine monophosphate, abbreviated as AMP.

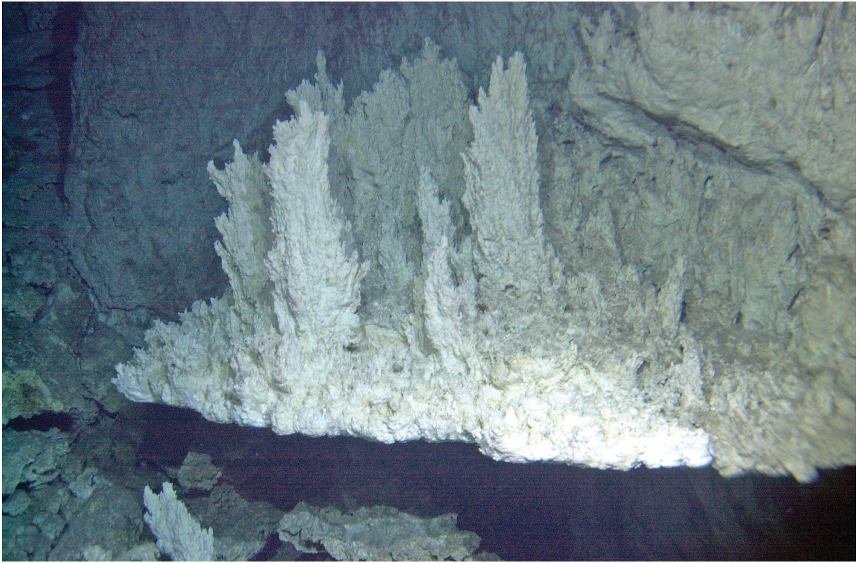

FIGURE 61 The Lost City alkaline hydrothermal vent field features a collection of about 30 carbonate chimneys each between 30–60 metres tall. This picture shows a five-foot-wide ledge on the side of a chimney which is topped with dendritic carbonate growths.

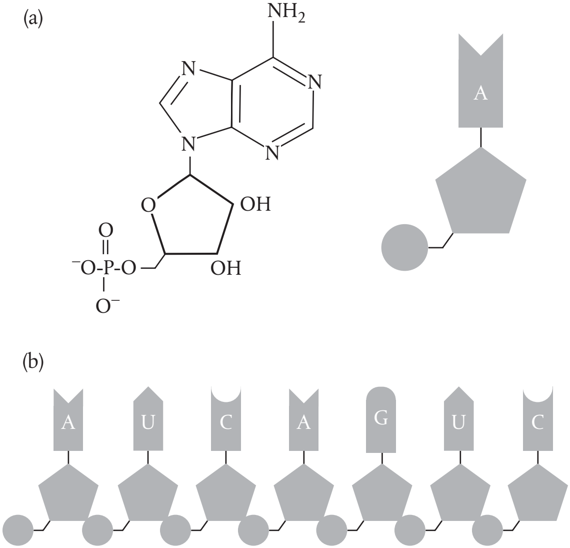

FIGURE 62 To simplify the depiction of the complex molecular structures involved in the chemistry of life we substitute simple geometric shapes to represent the different chemical sub-units. For example, in (a) the ribose unit of adenosine monophosphate is represented as a pentagon, and the phosphate unit as a circle. The adenine base is given a specific shape to distinguish it from guanine, uracil, and cytosine. When formed in sufficient quantities, the nucleotides polymerize to form RNA (b).

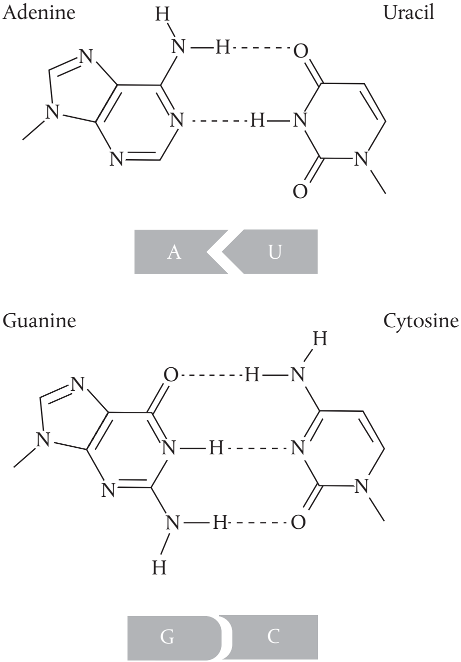

FIGURE 63 The electrons sitting in the molecular orbitals of the amine groups (—NH_2 and N—H) in both purines and pyrimidines are shared unequally, leaving the hydrogen atoms with a slight positive charge. These link up with lone pair electrons on the oxygen atoms of the carbonyl groups and the ring nitrogen atoms to form hydrogen bonds. Although these are much weaker than ordinary chemical bonds, they are sufficient to hold the structures together.

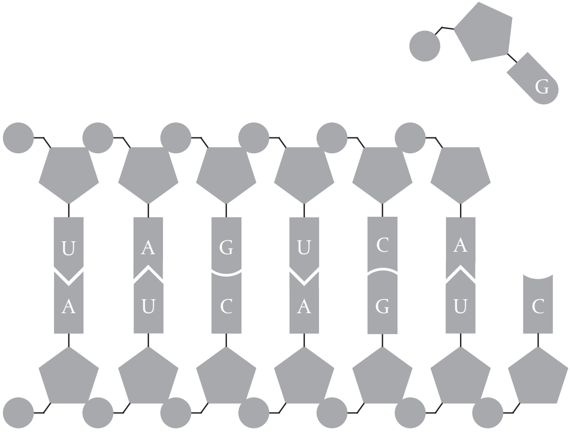

FIGURE 64 Hydrogen bonding between the complementary base pairs allows a strand of RNA to assemble a kind of photographic negative of itself in which A is replaced by U, C with G, etc. When these strands separate, the negative can go on to assemble another positive. In this way, a strand of RNA can catalyse its own replication.

<table>
<tr><th>First base</th><th colspan="4">Second base</th><th>Third base</th></tr>
<tr><th></th><th>U</th><th>C</th><th>A</th><th>G</th><th></th></tr>
<tr><td rowspan="4">U</td><td rowspan="2">Phenyl-alanine</td><td rowspan="4">Serine</td><td rowspan="2">Tyrosine</td><td rowspan="2">Cysteine</td><td>U</td></tr>
<tr><td>C</td></tr>
<tr><td rowspan="6">Leucine</td><td>STOP</td><td>STOP</td><td>A</td></tr>
<tr><td>STOP</td><td>Tryptophan</td><td>G</td></tr>
<tr><td rowspan="4">C</td><td rowspan="4">Proline</td><td rowspan="2">Histidine</td><td rowspan="4">Arginine</td><td>U</td></tr>
<tr><td>C</td></tr>
<tr><td rowspan="2">Glutamine</td><td>A</td></tr>
<tr><td>G</td></tr>
<tr><td rowspan="4">A</td><td rowspan="3">Isoleucine</td><td rowspan="4">Threonine</td><td rowspan="2">Asparagine</td><td rowspan="2">Serine</td><td>U</td></tr>
<tr><td>C</td></tr>
<tr><td rowspan="2">Lysine</td><td rowspan="2">Arginine</td><td>A</td></tr>
<tr><td>Methionine</td><td>G</td></tr>
<tr><td rowspan="4">G</td><td rowspan="4">Valine</td><td rowspan="4">Alanine</td><td rowspan="2">Aspartic Acid</td><td rowspan="4">Glycine</td><td>U</td></tr>
<tr><td>C</td></tr>
<tr><td rowspan="2">Glutamic Acid</td><td>A</td></tr>
<tr><td>G</td></tr>
</table>

FIGURE 65 The genetic code. Sequences of three base units in RNA, called *codons,* specify the sequence of amino acids that will be assembled to make proteins. There is considerable redundancy in the code, with many different three-letter codons specifying the same amino acids.

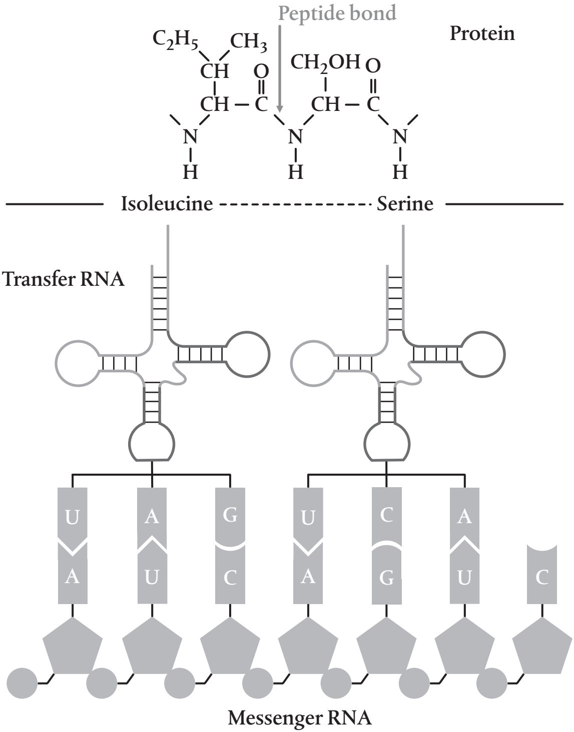

FIGURE 66 Each codon in the messenger RNA bonds with a corresponding anti-codon on the anti-codon arm of the transfer RNA (not drawn to scale in this figure). For example, the codon AUC bonds with the anti-codon UAG. From the genetic code in Figure 65 we know that AUC codes for the amino acid isoleucine, which bonds to the acceptor stem of the tRNA. The next codon AGU codes for serine. As the amino acids line up, they polymerize, forming peptide bonds between them. The sequence of amino acids then determines the properties and molecular geometry of the resulting protein.

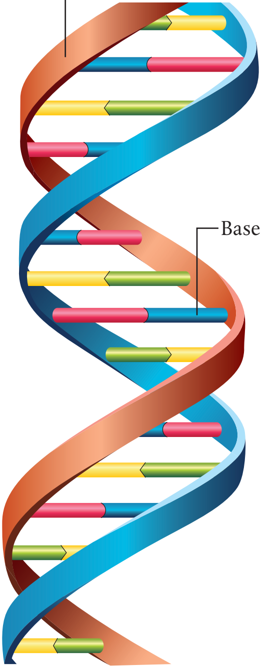

FIGURE 67 The iconic double helix structure of DNA was first elucidated in 1953 by James D. Watson, Francis Crick, Maurice Wilkins, and Rosalind Franklin. It consists of two spirals formed by two deoxyribose-phosphate 'backbones' tied together by hydrogen bonds between the base pairs adenine-thymine and guanine-cytosine.

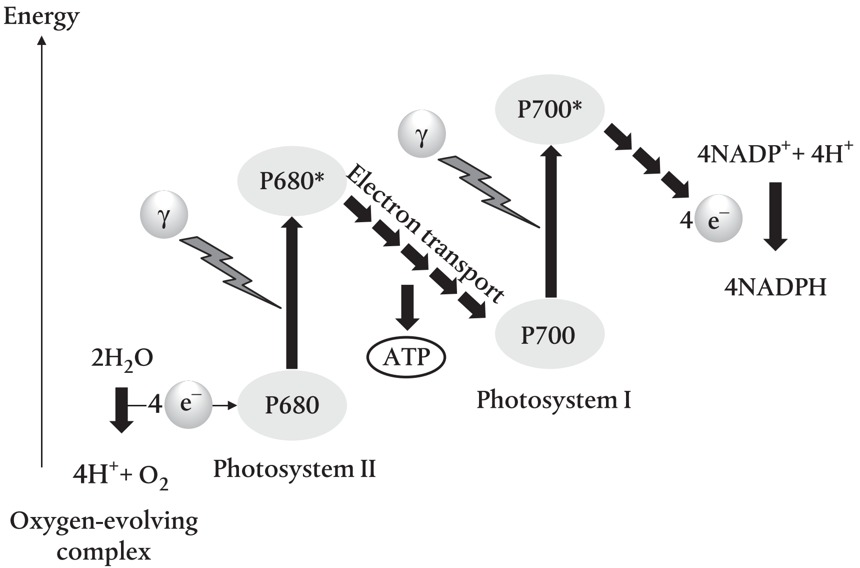

FIGURE 68 The 'Z-scheme' of photosynthesis, which uses light to fix carbon from CO_2 using water (H_2O) as the source of hydrogen. Molecular oxygen (O_2) is released as a waste by-product.

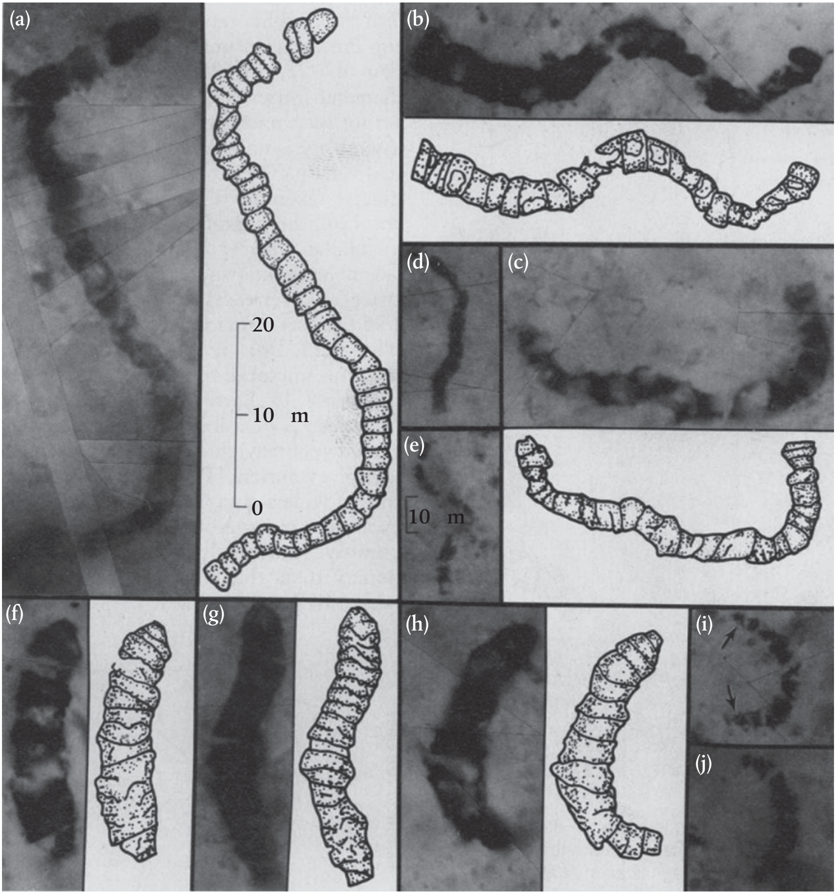

FIGURE 69 Schopf declared these structures, found in the Warrawoona chert, to be examples of *microfossils*, the fossilized remains of some of the earliest microscopic organisms. The drawing to the right of image (a) provides a scale, in which μm means micrometres, 10^{-6} metres. Schopf referred to these structures as 'cyanobacteria-like', but later accepted that there is insufficient evidence for this assertion. Today, there appears to be no consensus that these are genuine microfossils (some of the angles in the drawings appear more characteristic of crystal growth), although other evidence for early Archean organisms is still sound. Reproduced, with permission, from J. William Schopf, *Science*, **260** (1993), p. 643.

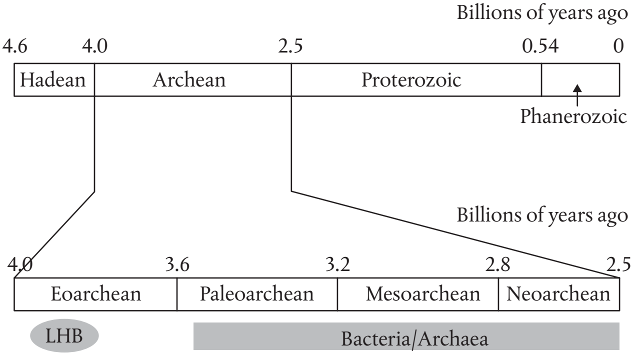

FIGURE 70 The Earth's geological timescale is split into a series of four eons—the Hadean, Archean, Proterozoic, and Phanerozoic. The Archean eon spans the time period from 4.0 to 2.5 billion years ago, and is further divided into a series of four 'eras'. These are the Eoarchean, Paleoarchean, Mesoarchean, and Neoarchean. The Late Heavy Bombardment (LHB) occurred in the Eoarchean era, about 3.8 billion years ago. The evidence from microbially induced sedimentary structures suggests that bacteria and archaea were already thriving by the early Paleoarchean era.

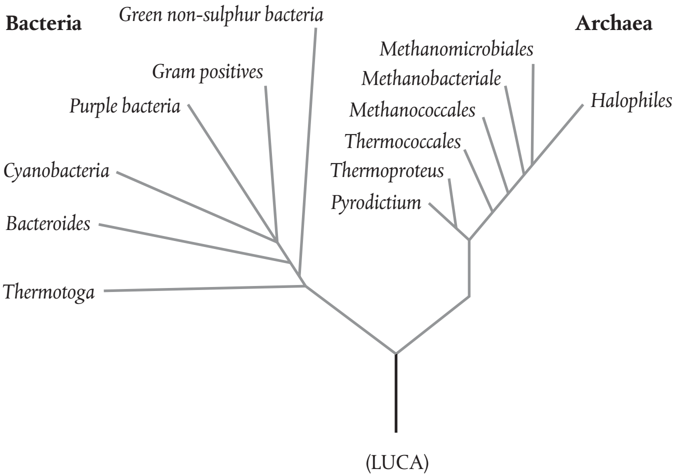

FIGURE 71 The first phylogenetic ‘tree of life’ was published by Carl Woese and his colleagues in 1990. The order of branching and the lengths of the branches reflect the ‘relatedness’ of different life forms based on rRNA sequence comparisons. Note that only two domains are shown here (see Chapter 10 for the full story). Adapted from Carl R. Woese, Otto Kandler, and Mark R. Wheelis, *Proceedings of the National Academy of Sciences*, **87** (1990), p. 4578.

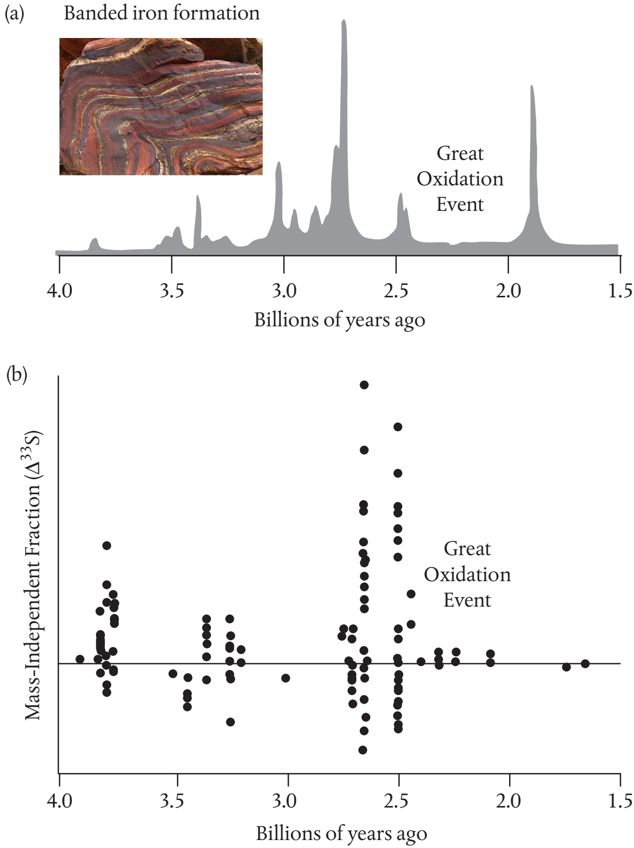

FIGURE 72 (a) Banded iron formations (BIFs) are produced by iron oxide (rust) formed in the reaction of dissolved iron and molecular oxygen. Studies of BIFs suggest that these occurred fairly regularly throughout the early history of the Earth, but stopped suddenly about 2.4 billion years ago. This is believed to have been due to the accelerated oxygenation of the atmosphere and oceans in the Great Oxidation Event. A number of explanations have been suggested for the deposition that occurred 1.8 billion years ago, and this likely reflects tectonic movements as much as anything. The mass-independent fraction (MIF) of ^{33}S varies through geological time until 2.4 million years ago, when it falls to zero (b). This is believed to signal the formation of a protective ozone layer in the stratosphere, shielding the Earth from the Sun's ultraviolet light.

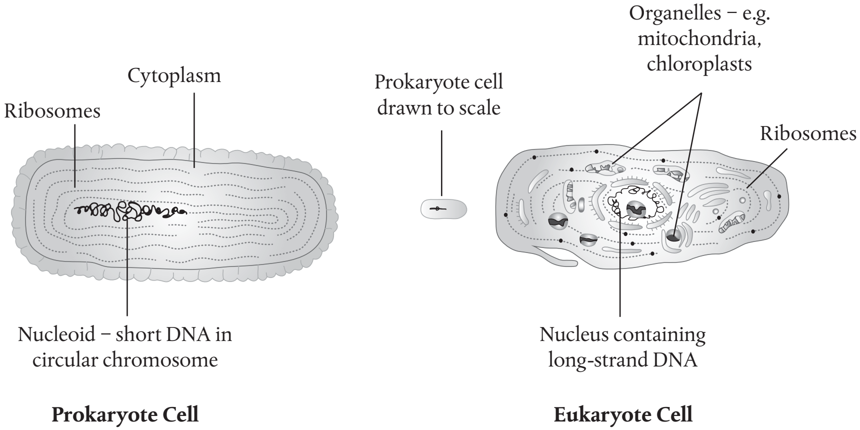

FIGURE 73 Comparison of prokaryote and eukaryote cells. Prokaryotes are typically 0.2–1.0 microns in length and possess a simple cell structure consisting of a short length of DNA, typically formed into a circular chromosome and ribosomes—small protein manufacturing complexes in a cytoplasm which consists of about 80% water. Eukaryotes are much larger, being 1–10 microns in length with a much more complex internal structure consisting of a nucleus, organelles (such as mitochondria and chloroplasts), ribosomes, cytoplasm, and more.

---

* To put this in perspective, note that every human cell contains roughly two metres of DNA.

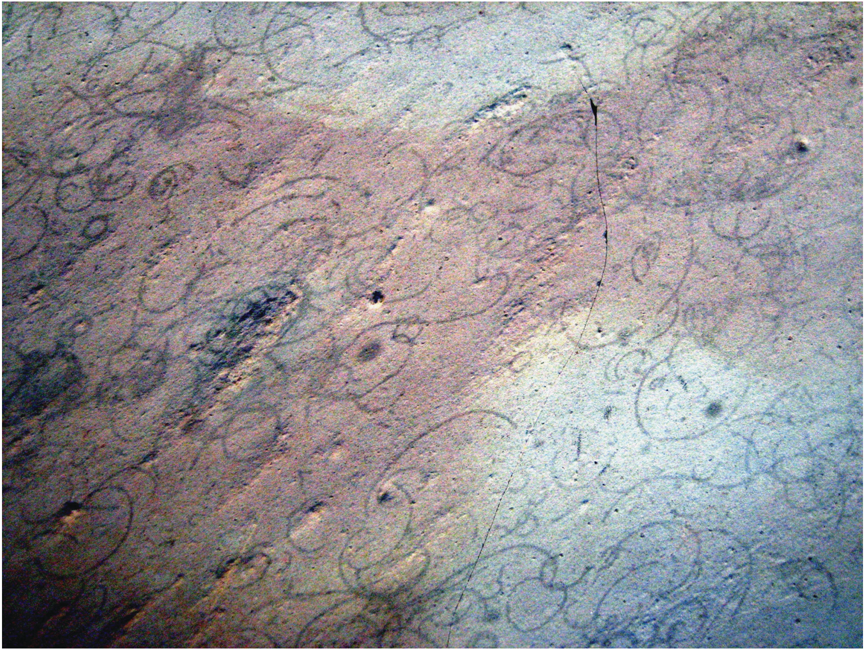

FIGURE 74 Fossil evidence for *Grypania spiralis,* thought to be a 1.9 billion year old multicellular alga, from the Negaunee Iron Formation in Michigan's Upper Peninsula. These ribbon-like fossils measure a few millimetres in width and up to 10 centimentres in length.

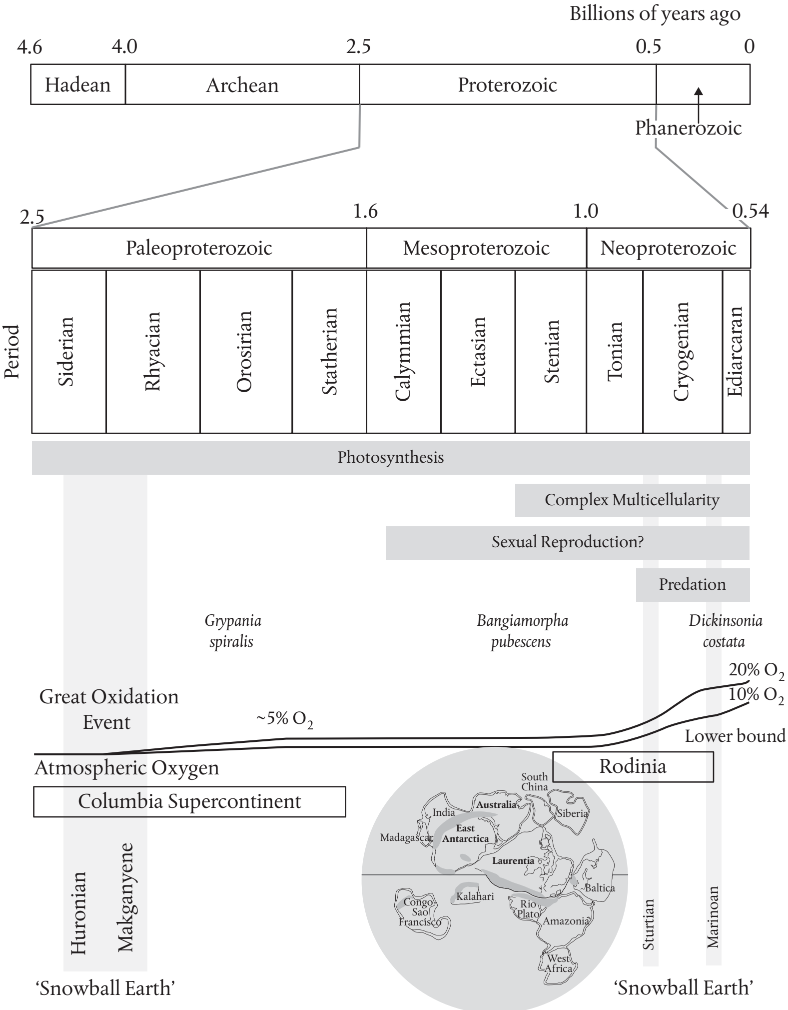

FIGURE 75 An attempt to map evolutionary inventions, selected fossil organisms, and geological events against the geological timescale of the Proterozoic eon. Evolution accelerates the development of diversity, leading eventually to the first animals, as a result of changes in the assembly of Earth's continents, the rise of oxygen in the atmosphere and oceans, and 'Snowball Earth' episodes.

FIGURE 76 *Fractofusus misrai* is named for the Indian geologist Shiva Balak (SB) Misra who was a graduate student when he discovered a rich assemblage of Ediacaran fossils at Mistaken Point in Newfoundland, Canada, in June 1967. The area where this picture was taken is now carefully protected, and forms part of the Mistaken Point Ecological Reserve. This fossil is about 10 centimetres in length, and 565 million years old.

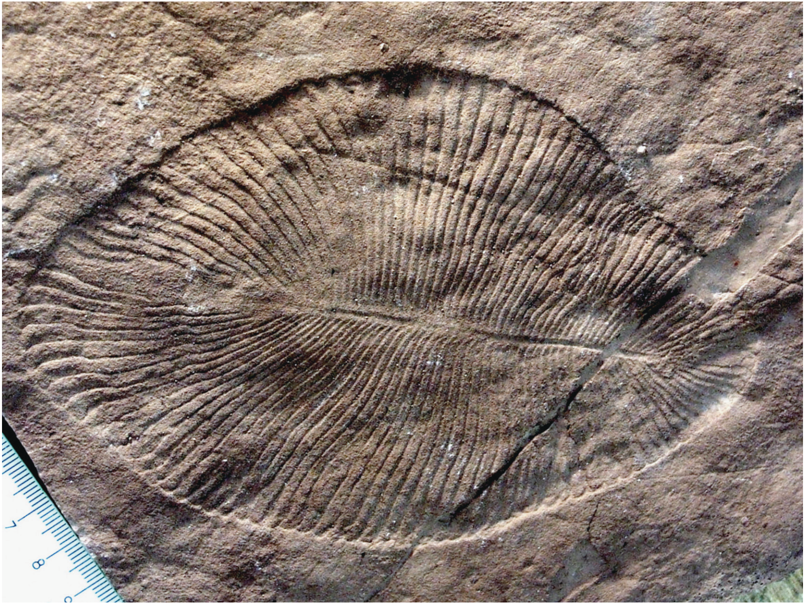

FIGURE 77 *Dickinsonia costata* was discovered in the Ediacara Hills in Southern Australia in 1947. It is thought that these were primitive cnidarians, a phylum that includes jellyfish, corals, and sea anemones that lived in colonies. Whatever they were, they didn't survive much beyond the end of the Ediacaran period.

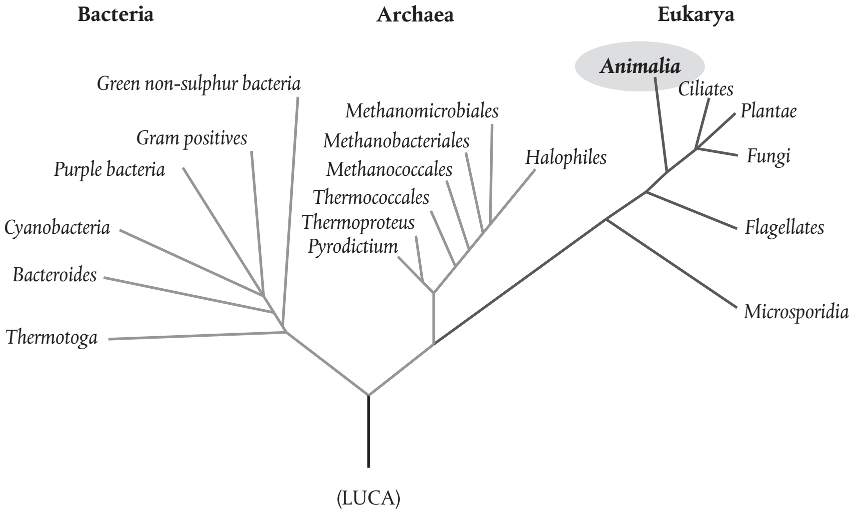

FIGURE 78 The full phylogenetic 'tree of life' published by Carl Woese and his colleagues in 1990 includes the Eukarya, shown here on the right. Animalia (animals), Plantae (plants), and Fungi are kingdoms in the domain of Eukarya and are reasonably self-explanatory. However, you may be unfamiliar with Ciliates, a group of single-celled eukaryotes that possess hair-like organelles called cilia. Flagellates are eukaryote cells possessing a whip-like structure called a flagellum which the organism uses to move around (think of male sperm cells). The Microsporidia are single-celled fungal parasites. Recall from Figure 71 that the order of branching and the lengths of the branches reflect the genetic 'relatedness' of different lifeforms based on rRNA sequence comparisons. This diagram was the first of its kind but has now been superseded by studies based on many more organisms and more gene sequences, and the details of eukaryote evolution are now accepted to be rather different. However, the late appearance of plants and animals holds firm. Adapted from Carl R. Woese, Otto Kandler, and Mark R. Wheelis, *Proceedings of the National Academy of Sciences*, **87** (1990), p. 4578.

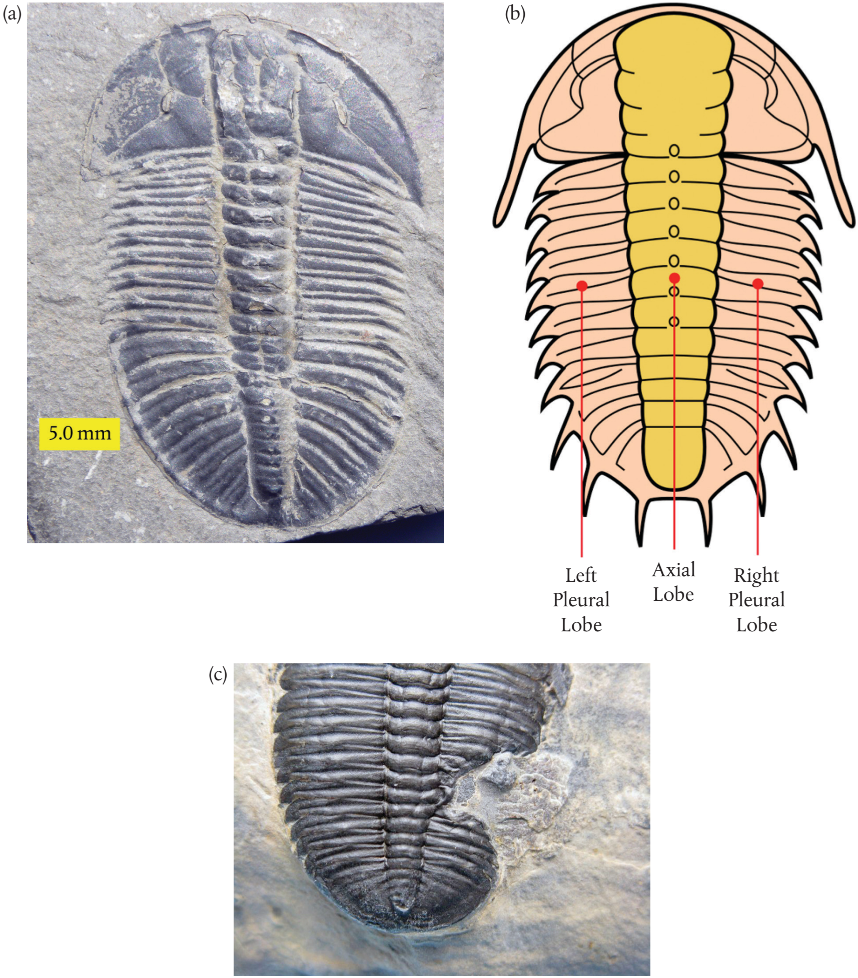

FIGURE 79 (a) A fossil trilobite from the mid-Cambrian. (b) Schematic showing the main exterior parts. (c) This trilobite carries a prominent bite mark.

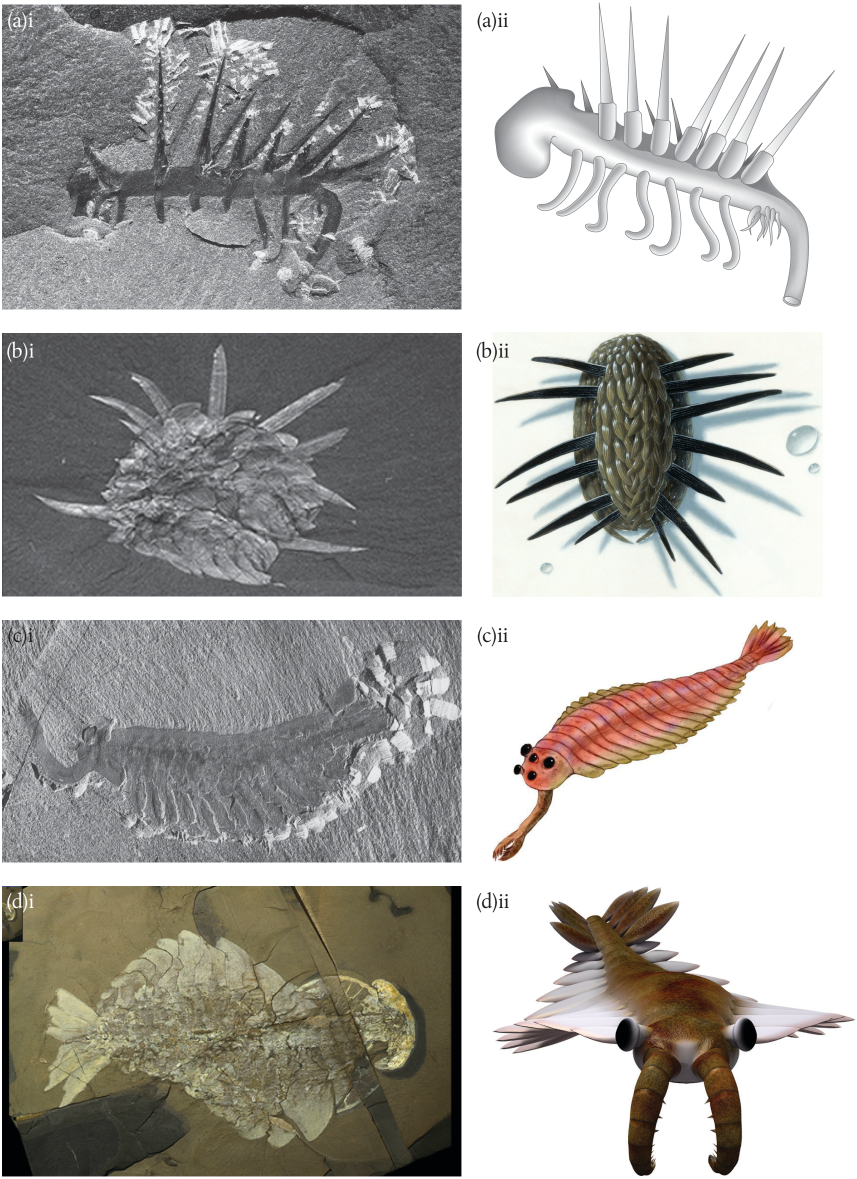

FIGURE 80 Examples of Cambrian marine animals discovered in the fossils of the Burgess Shale. (a) *Hallucigenia sparsa*, showing an example fossil specimen on the left and an artist's reconstruction on the right. (b) *Wiwaxia corrugata*. (c) *Opabinia regalis*. (d) *Anomalocaris canadensis*.

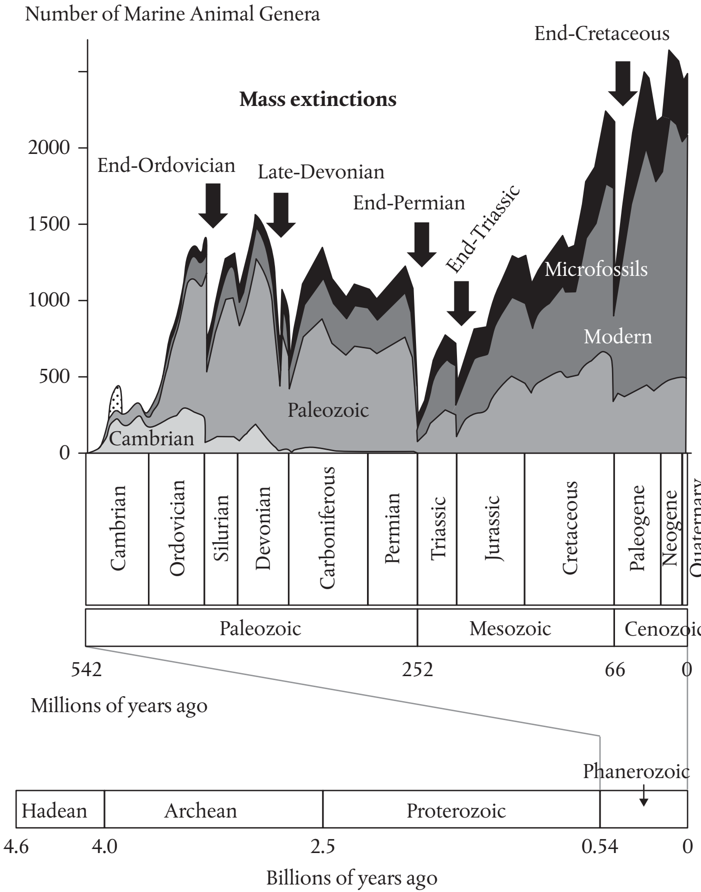

FIGURE 81 The evolution of marine animal genera from the beginning of the Cambrian period to the present, deduced from the fossil record. While marine life has become more diverse over time (the number of genera has increased) the pattern is punctuated by a series of dramatic and rapid declines, corresponding to mass extinctions. The 'big five' mass extinctions are marked with arrows. Adapted from Sepkoski's Online Genus Database: http://strata.geology.wisc.edu/jack/

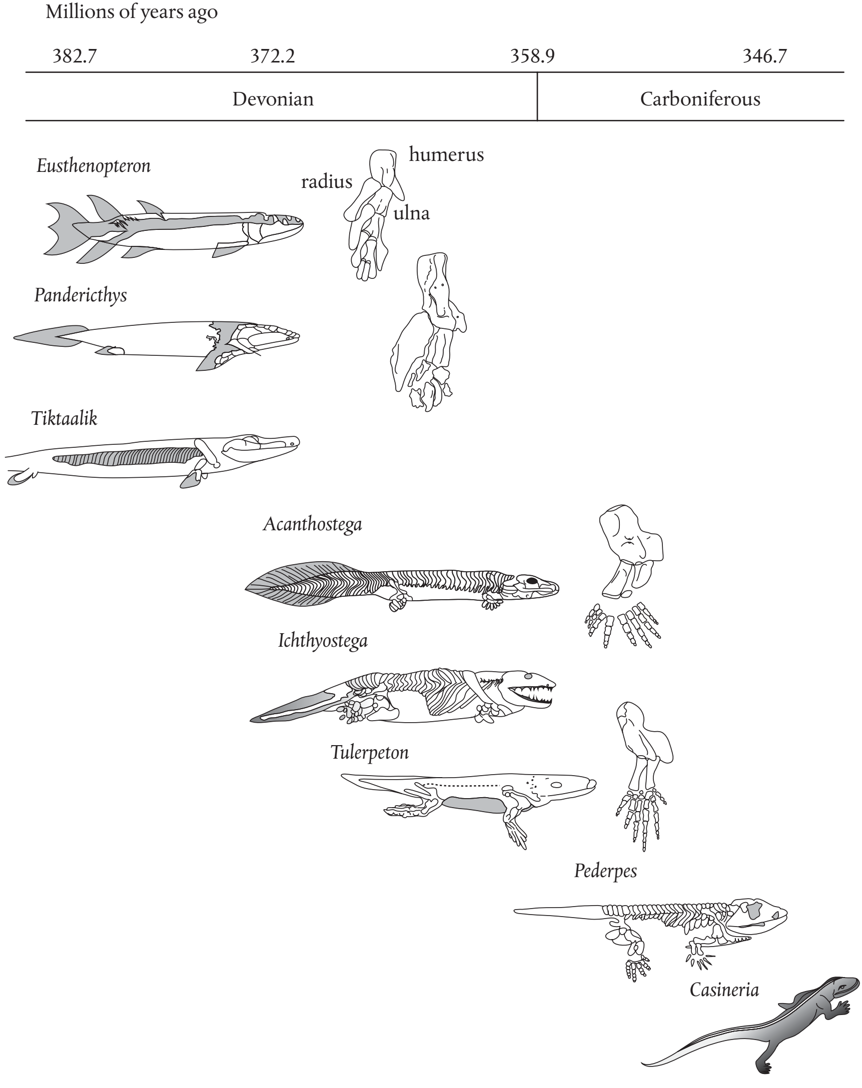

FIGURE 82 The transition from lobe-finned fish to tetrapod was likely complex, involving the evolution of fins into limbs with digits, and the development of anatomical structures adapted to walking. The fossil record reveals a range of creatures, called tetrapodomorphs, with morphologies in a spectrum ranging from tetrapod-like fish to fish-like tetrapods. *Casineria* was a fully fledged land-living tetrapod, dated to 340 million years ago. This figure has been put together from Figures 1, 5, and 12 in Jennifer A. Clack, *Evolution: Education & Outreach*, **2** (2009), pp. 213–223.

FIGURE 83 The supercontinent of Pangaea was formed about 300 million years ago, towards the end of the Carboniferous. It was assembled from Gondwana (South America, Africa, India, Australia, and Antarctica), Euramerica—consisting of Laurentia (North America) and Baltica (Europe), and Siberia. It stretched from pole to pole, with much of the landmass in the southern hemisphere.

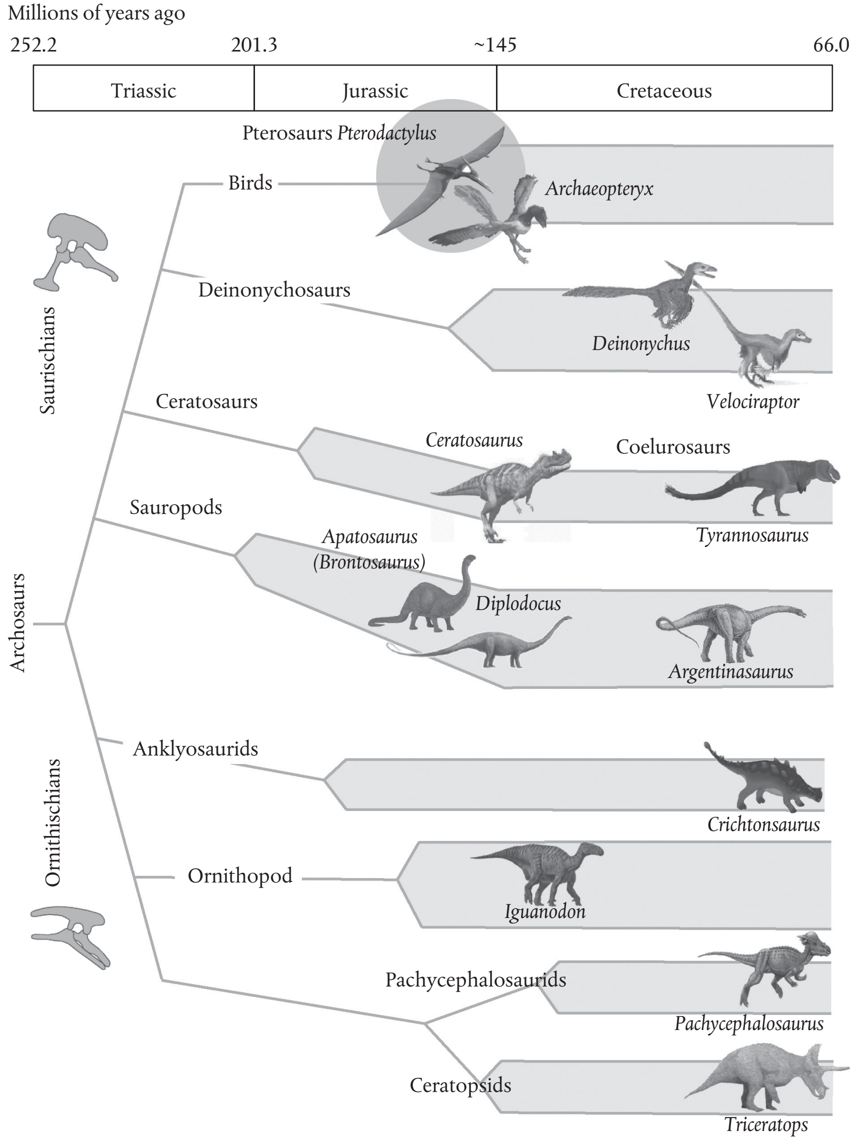

FIGURE 84 An approximate description of the evolution of dinosaurs, from their lowest common ancestor at the beginning of the Triassic to the end of the Cretaceous. Dinosaurs are categorized by their hip bones into saurischians ('lizard-hipped') and ornithischians ('bird-hipped'). Although many of the various orders of dinosaur may be unfamiliar, each is illustrated with a more familiar genus. One exception is *Pterodactylus*, which is not considered to be a dinosaur (and is thus marked by a grey circle) but is included here to illustrate the evolution of flight.

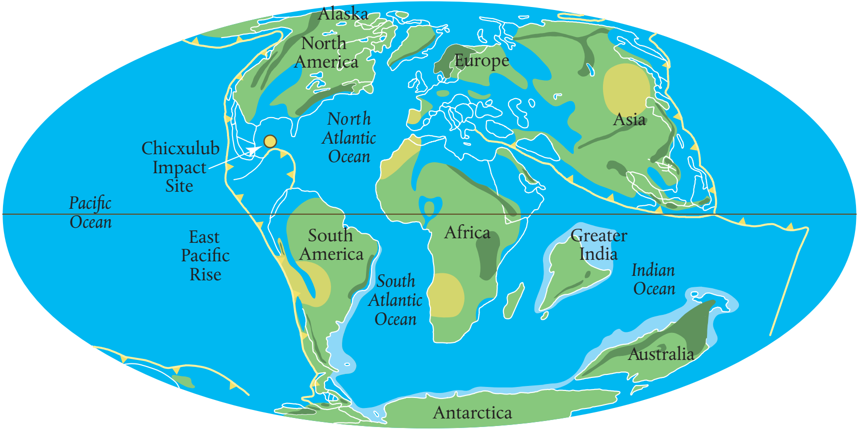

FIGURE 85 The Chicxulub impact site, as it would appear on the late-Cretaceous Earth. Laurentia has now rifted from Eurasia, opening up the North Atlantic Ocean. Gondwana has broken up, with South America rifting from Africa to form the South Atlantic Ocean. India is making its way northwards to collide with southern Asia. Australia is still connected with Antarctica but will soon break free and head northwards.

---

* At the time, this geological boundary was between the Cretaceous and Tertiary periods and referred to as the K-T boundary. The Tertiary is no longer recognized by the International Commission on Stratigraphy.

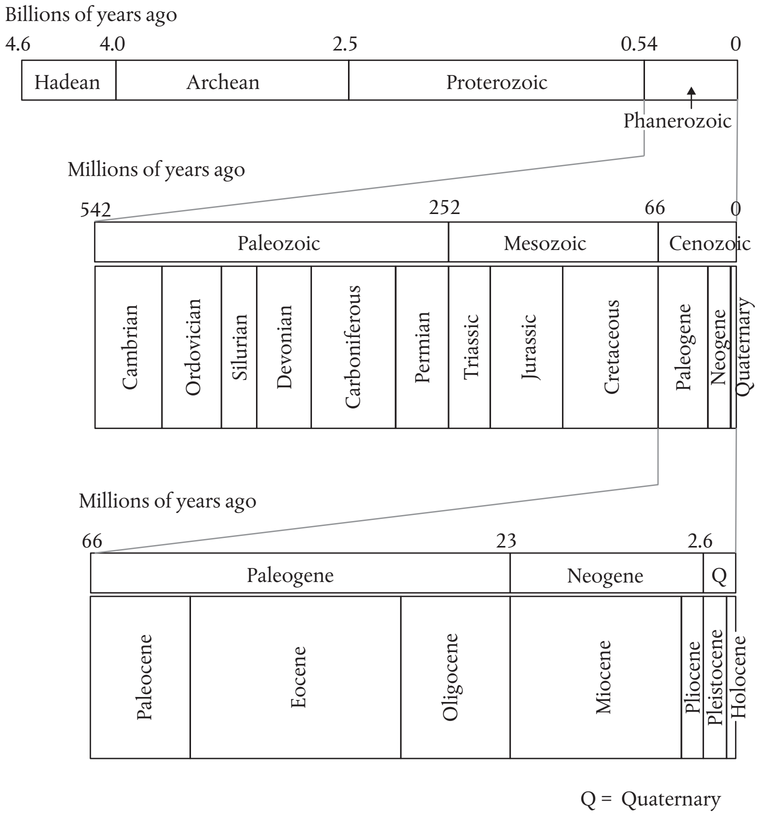

FIGURE 86 As we get closer to the time frame of human evolution, the geological timescale becomes more compressed. The Phanerozoic eon begins 542 million years ago and continues to the present day. This, in turn, is divided into eras, including the Paleozoic, Mesozoic, and Cenozoic. We have been following events thus far in relation to the successions of periods within these eras, from the Cambrian to the Paleogene, Neogene, and Quaternary. We now split each of these latter periods of the Cenozoic into epochs—the Paleogene into Paleocene, Eocene, and Oligocene; the Neogene into Miocene and Pliocene, and the Quaternary into Pleistocene and Holocene.

(a) (b)

FIGURE 87 Hurum and his colleagues argued that fossil Ida (*Darwinius masillae*), image, (a) is a strepsirrhine primate with some of the characteristics of early haplorrhines, making it a kind of 'missing link' between the two primate sub-orders. The scientific consensus is that Ida is a strepsirrhine related to modern lemurs with nothing to tell us about the evolution of haplorrhines (and monkeys and apes).

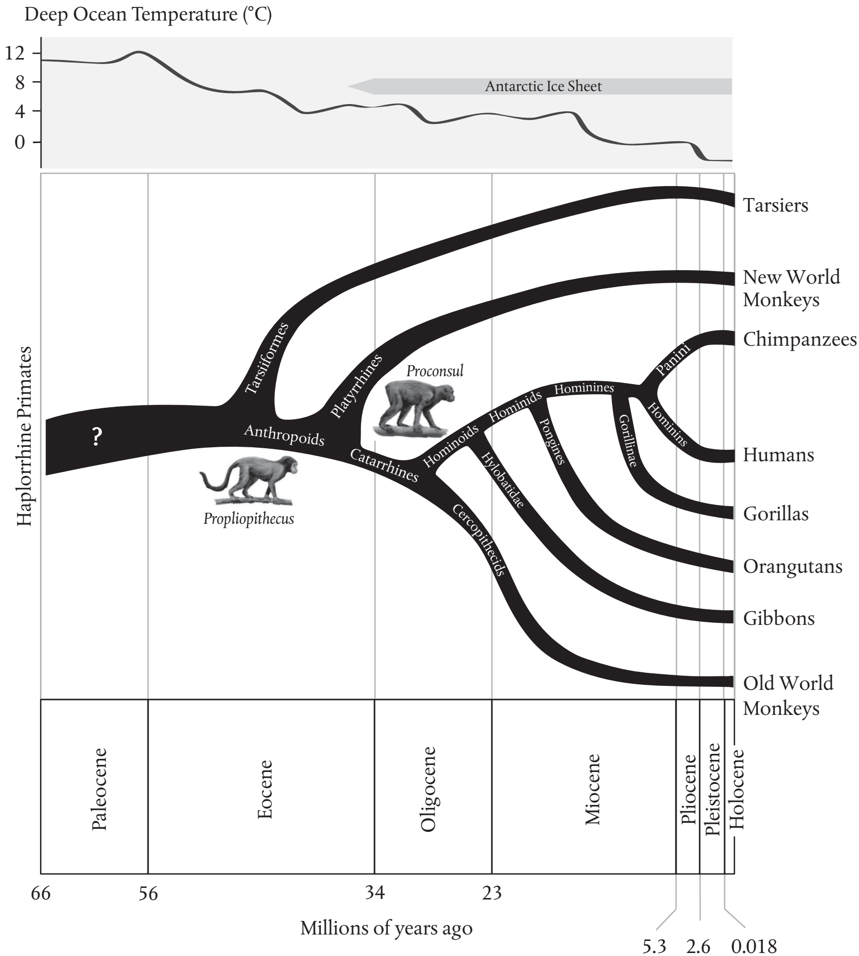

FIGURE 88 The evolution of haplorrhine primates from the beginning of the Paleocene to the present day. As there is little fossil evidence from the Paleocene, this section of the trunk of the evolutionary tree is labelled with a question mark (one estimate dates the divergence of haplorrhines and strepsirrhines to about 63 million years ago). The nature, location, and timing of these evolutionary divergences is strongly dependent on the global climate and, as temperatures decline from the end of the Paleocene (represented here in terms of deep ocean temperatures based on studies of oxygen isotope ratios), the tropical forests (and their primate inhabitants) retreat to Africa and parts of Asia.

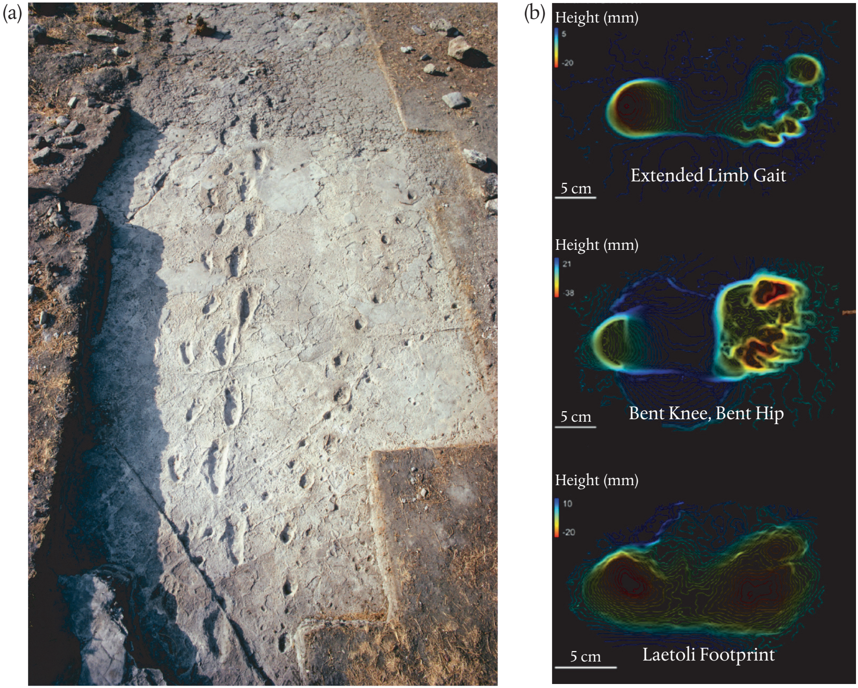

FIGURE 89 The Laetoli footprints (a) are approximately 3.6 million years old, caught in wet volcanic ash that hardened before being covered and preserved by fresh layers of ash. They are believed to have been made by three hominins of the species *Australopithecus afarensis*. (b) shows three-dimensional scans of experimental footprints made by a modern human walking with a regular, extended limb gait and with a more ape-like bent knee, bent hip gait (think chimpanzee). Note how the ape-like gait makes much deeper depressions particularly around the toes. These are compared with a similar three-dimensional scan of a Laetoli footprint. The gait appears to be much more human-like than ape-like. Adapted from David A. Raichlen, Adam D. Gordon, William E. H. Harcourt-Smith, Adam D. Foster, and Wm. Randall Haas, Jr., *PLoS ONE*, **5** (2010) e9769.

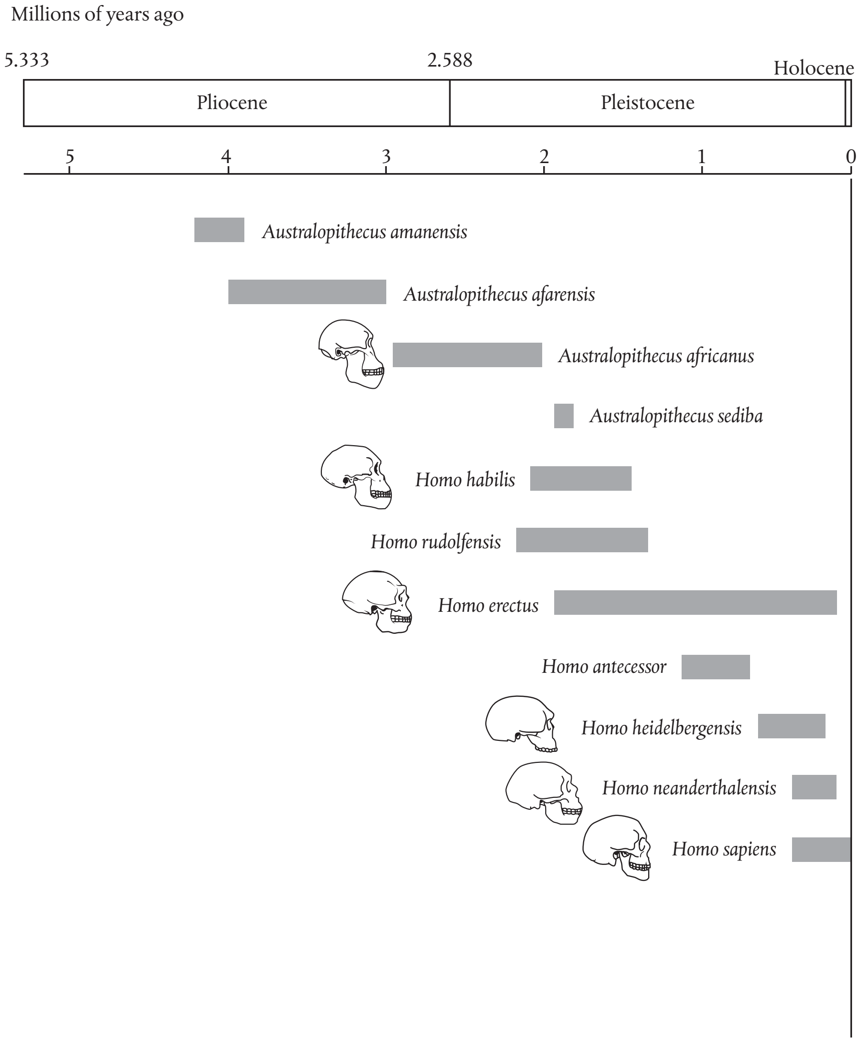

FIGURE 90 Approximate date ranges of fossil specimens for the principal species involved in the story of human evolution through the Pliocene and Pleistocene.

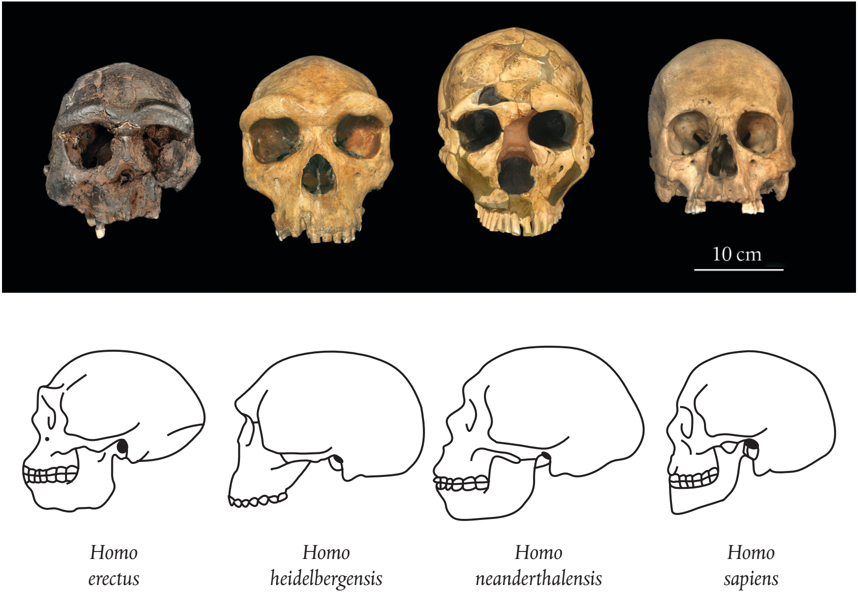

FIGURE 91 The bones never lie. Comparison of fossil skulls of Asian *Homo erectus* (specimen Sangiran 17 from Java, determined to be about 700 000 years old), African *Homo heidelbergensis* (Broken Hill 1, Zambia, about 300 000 years old), European *Homo neanderthalensis* (La Ferrassie 1, France, perhaps 70 000 years old), and Asian *Homo sapiens* (a modern human skull from Polynesia).

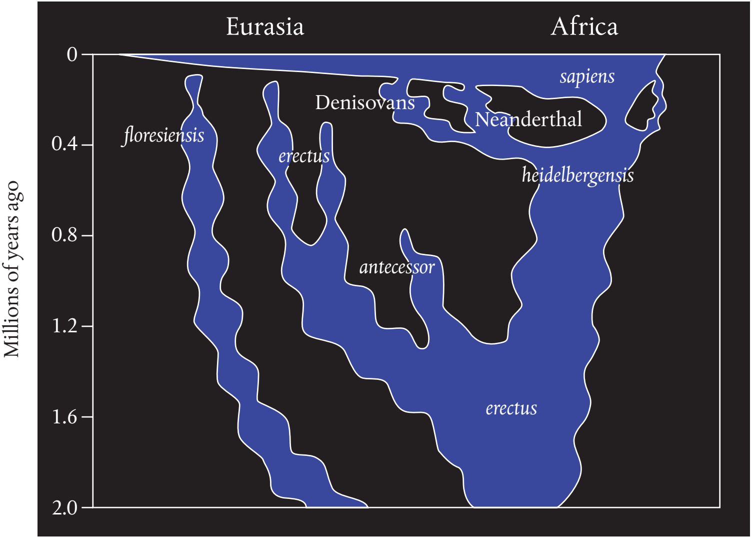

FIGURE 92 A tree diagram describing the history of recent human evolution over the past 2 million years based on both fossil evidence and DNA research, and the distribution of humans across Africa and Eurasia. The origin of *Homo floresiensis* is uncertain, but the species may have descended from *Homo erectus* or an earlier hominin species.

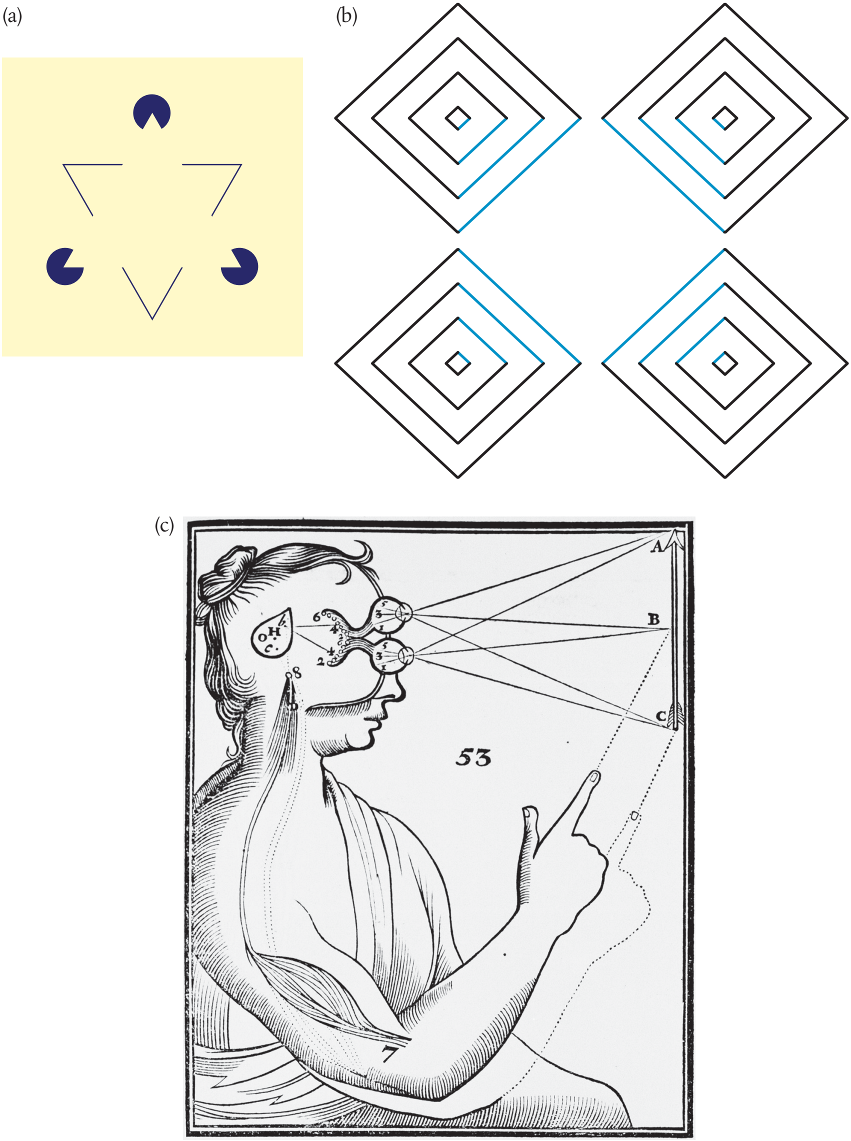

FIGURE 93 The Kanizsa triangle, first described by Italian psychologist Gaetano Kanizsa in 1955 (a) and the square neon colour spread (b) are examples of cognitive fiction illusions—our P-consciousness is tricked into perceiving geometrical objects that aren't there. Descartes argued that his senses cannot be trusted to deliver a faithful representation of the external physical world. He went on to argue that mind and body are distinct and separate substances, capable of independent existence. He identified the pineal gland at the centre of the brain as the 'seat' of consciousness, the place where the unphysical mind interacts with the physical brain (c).

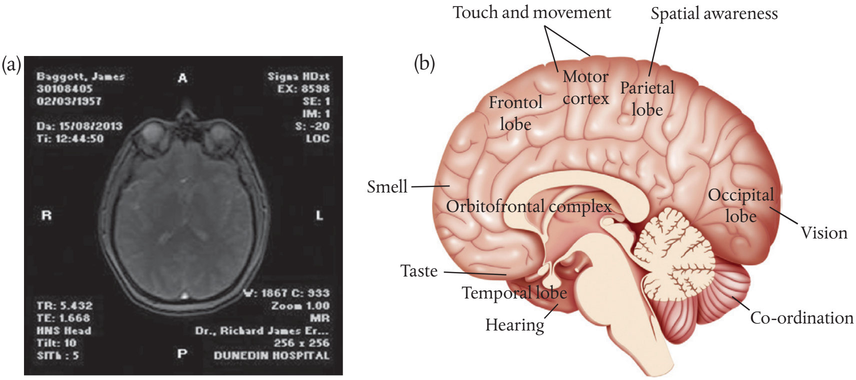

FIGURE 94 I had cause to have an MRI scan in August 2013, (a). This image shows the bilateral symmetry of my brain, with near-equal left and right hemispheres, and some hints of structure (called the limbic system) in the centre. Neuroscientists have mapped those parts of the brain cortex that are involved in sensory perception of the kind involved in P-consciousness (b). Much of the cortex is deployed in the tasks of sensing the external physical world, with the frontal lobe involved in higher-level processing of the kind required by A-consciousness.

(a)

(b)

FIGURE 95 Phineas Gage, pictured here (a) in a daguerreotype, suffered a terrible injury in 1848 while working for the Rutland and Burlington Railroad. An iron rod was blasted up through his left cheek, through his brain's frontal lobe and out the top of his head. Computer simulations performed some 120 years later (b) allowed Antonio Damasio and his colleagues to determine which parts of his brain had been damaged. Gage survived the accident, but damage to his frontal lobe changed his personality.

FIGURE 96 (a) Markings in red ochre (an iron-rich mineral) are thought to be the earliest examples of abstract expression by humans. Examples were discovered in Blombos Cave in South Africa and are between 70 000 and 100 000 years old. After the Great Leap Forward, thought to have occurred between 40 000 and 50 000 years ago, such expression reaches new heights, for example in paintings found in Chauvet Cave in southern France (b), determined to be 35 000 years old. Although most of the examples of this flowering of human creativity are found in Europe, examples have recently been discovered in Asia, such as these hand stencils found in a cave system in Sulawesi, Indonesia (c). Ritual burials at Sungir in Russia, dated at 28 000 to 30 000 years old, show rapidly developing craftwork (d). This adult male was buried in clothing decorated with 3000 beads.

TABLE 3: Positive powers of ten

Number	Name	Power of Ten	Prefix	Symbol
1	One	10^0		
10	Ten	10^1	deca	da
100	Hundred	10^2	hecto	h
1000	Thousand	10^3	kilo	k
1 000 000	Million	10^6	mega	M
1 000 000 000	Billion	10^9	giga	G
1 000 000 000 000	Trillion	10^{12}	terra	T

The speed of light, c, is measured to be 299 792 458 metres per second, which we can write as 299.792458 million metres per second or 2.99792458×10^8 metres per second.

TABLE 4: Negative powers of ten

Number	Name	Power of Ten	Prefix	Symbol
0.1	Tenth	10^{-1}	deci	d
0.01	Hundredth	10^{-2}	centi	c
0.001	Thousandth	10^{-3}	milli	m
0.000001	Millionth	10^{-6}	micro	μ
0.000000001	Billionth	10^{-9}	nano	n
0.000000000001	Trillionth	10^{-12}	pico	p

Excited hydrogen atoms emit red light with a wavelength of 656.28 nanometres (this is the so-called Hα line). We can re-express this number as 656.28 billionths of a metre, 656.28×10^{-9} metres or 6.5628×10^{-11} metres.

	Mass	Orbital Radius	Orbital Period	L	% of Total L
	10^{24}kg	10^{6}km	Days	10^{43}kgm²/s	
Mercury	0.33	57.91	87.97	0.0001	0.00%
Venus	4.87	108.21	224.70	0.0018	0.06%
Earth	5.97	149.51	365.26	0.0027	0.08%
Mars	0.64	227.94	686.97	0.0004	0.01%

(*continued*)

(continued)

	Mass	Orbital Radius	Orbital Period	L	% of Total L
	10^{24}kg	10^6km	Days	10^{43}kgm²/s	
Jupiter	1868.60	778.57	4332.59	1.9012	58.44%
Saturn	586.46	1,433.45	10,579.22	0.8145	25.04%
Uranus	86.81	2876.68	30,799.10	0.1696	5.21%
Neptune	102.43	4503.44	60,193.03	0.2510	7.71%

Note that in performing these calculations, we need to turn kilometres into metres and days into seconds. For a uniform solid sphere, $I=\left(\frac{2}{5}\right)mr^2$ and so for the spin motion of the Sun around its axis we have $L=\left(\frac{4\pi}{5}\right)mr^2/T$. If we look up the values of the mass, radius, and sidereal rotation period of the Sun we get:

	Mass	Radius	Rotation Period	L	% of Total L
	10^{24}kg	10^6km	Days	10^{43}kgm²/s	
Sun	1.99×10^6	0.70	25.05	0.1120	3.44%

The total angular momentum of the solar system is the sum of these values of *L* and is equal to 3.25×10^{43} kgm²/s. These calculations show that although the Sun accounts for 99.9% of the total mass of the solar system, it has only 3.4 per cent of the total angular momentum.

We can ask what the rotation period of the Sun would need to be in order for it to account for 99.9% of the total angular momentum. In this case, the total angular momentum of the eight planets (3.14×10^{43} kgm²/s) accounts for just 0.1% of the total, requiring the Sun to have $L = 3.15 \times 10^{46}$ kgm²/s. Rearranging the equation for *L* gives $T=\left(\frac{4\pi}{5}\right)mr^2/L$, from which we deduce that *T* would need to be 77 seconds.

6 The relationship between luminosity and surface temperature is given by $L = 4\pi R^2 \sigma T_{eff}^4$, where *L* is the luminosity of the star, *R* is the radius, T_{eff} is the effective surface temperature and σ is the Stefan–Boltzmann constant, a constant of proportionality between the energy radiated by a black body per unit surface area and its temperature, with a value of about 5.67×10^8 Wm⁻²T⁻⁴.

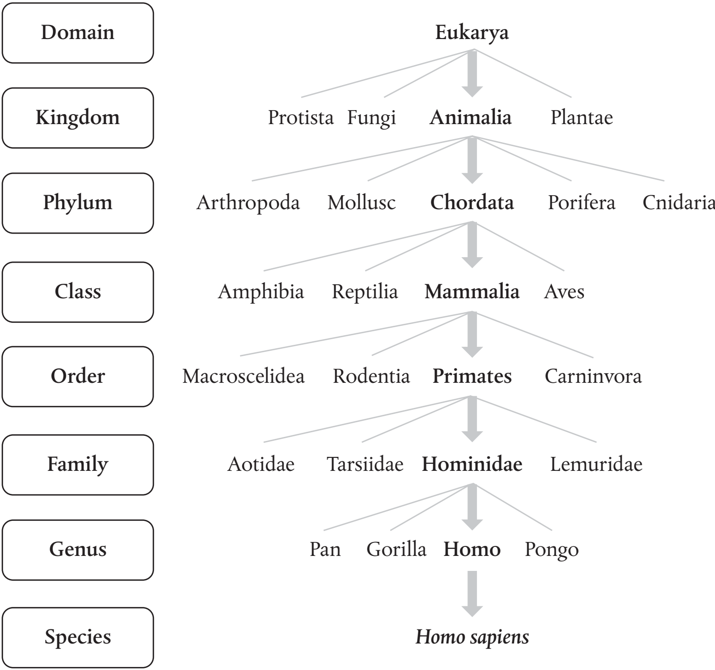

FIGURE 97 The system of biological taxonomy from Domain to Species.